

Global 2-cluster dynamics under large symmetric groups

Bernold Fiedler*, Sindre W. Haugland**,
Felix Kemeth***, Katharina Krischer**

version of August 24, 2020

*

Institut für Mathematik
Freie Universität Berlin
Arnimallee 3
14195 Berlin, Germany

**

Institut für Physik
Technische Universität München
James-Franck-Straße 1
85748 Garching, Germany

Department of Chemical and Biomolecular Engineering
Whiting School of Engineering
Johns Hopkins University
3400 North Charles Street
Baltimore, MD 21218, USA

Abstract

We explore equivariant dynamics under the symmetric group S_N of all permutations of N elements. Specifically we study cubic vector fields which commute with the standard real $(N - 1)$ -dimensional irreducible representation of S_N .

All stationary solutions are cluster solutions of up to three clusters. The resulting global dynamics is of gradient type: all bounded solutions are cluster equilibria and heteroclinic orbits between them. In the limit of large N , we present a detailed analysis of the web of heteroclinic orbits among the plethora of 2-cluster equilibria. Our focus is on the global dynamics of 3-cluster solutions with one rebel cluster of small size. These solutions describe slow relative growth and decay of 2-cluster states.

Applications include oscillators with all-to-all coupling and electrochemistry. For illustration we consider synchronization clusters among N Stuart-Landau oscillators with complex linear global coupling.

Contents

1	Introduction	1
2	Cluster dynamics	5
3	The limit of large symmetric groups S_N	7
4	Two-cluster dynamics	8
4.1	The degenerate transition case $c = -1$	10
4.2	The case $c < -1$	10
4.3	The case $c > -1$	13
5	Rebel dynamics and blocking	15
6	Results	23
6.1	The case $-\infty < c < -2$	23
6.2	The case $-2 < c < -3/2$	26
6.3	The case $-3/2 < c < -4/3$	26
6.4	The case $-4/3 < c < -5/4$	28
6.5	The case $-5/4 < c < -1$	28
6.6	The case $-1 < c < -1/2$	30
6.7	The case $-1/2 < c < +\infty$	30
7	Example: Stuart-Landau oscillators with global coupling	31

1 Introduction

Networks of identical oscillators with global all-to-all coupling are a ubiquitous source of dynamical systems which are equivariant under the *symmetric group* S_N of all permutations of N elements $\{1, \dots, N\}$.

In section 7 below, we address the specific example of coupled Stuart-Land oscillators. See also the companion paper [KHK19]. We will eliminate a global averaged phase oscillation. Near the trivial periodic solution of total synchrony, we consider loss of synchrony, and of stability, by bifurcation at a zero transverse eigenvalue. We reduce the complex ODE dynamics from $\mathbb{C}^N = \mathbb{R}^{2N}$ to a local center manifold of real dimension $N - 1$. In particular we study the resulting reduced dynamics of 2-cluster solutions and their heteroclinic transitions, up to and including third order. Our main tool will be equivariance under the permutation group S_N .

For a general background on dynamics and equivariance see for example [GoSt86, GoSt02, GuHo83, Van82]. For a background on S_N -equivariance see [Elm01, GoSt02, SEC03].

Permutations $\pi \in S_N$ act linearly on vectors $\mathbf{x} \in X := \mathbb{R}^N$ by permutations of their components x_n . This linear representation of S_N is given by

$$(1.1) \quad (\pi \mathbf{x})_n := x_{\pi^{-1}(n)}.$$

Group *invariants* $I : \mathbb{R}^N \rightarrow \mathbb{R}$ satisfy

$$(1.2) \quad I(\pi \mathbf{x}) = I(\mathbf{x})$$

for all $\pi \in S_N$ and all $\mathbf{x} \in \mathbb{R}^N$, by definition. The ring of polynomial S_N invariants I is freely generated by the power sums

$$(1.3) \quad p_m := \sum_{n=1}^N x_n^m,$$

for $m = 1, \dots, N$. We may subsume the case of constant I as $m = 0$.

Equivariant vector fields $\mathbf{f} : \mathbb{R}^N \rightarrow \mathbb{R}^N$, here under the group S_N , commute with the linear group action:

$$(1.4) \quad \mathbf{f}(\pi \mathbf{x}) = \pi \mathbf{f}(\mathbf{x}),$$

for all $\pi \in S_N$ and all $\mathbf{x} \in \mathbb{R}^N$. For Lipschitz continuous \mathbf{f} , the solutions $\mathbf{x} = \mathbf{x}(t)$ of the associated ordinary differential equation (ODE)

$$(1.5) \quad \dot{\mathbf{x}} = \mathbf{f}(\mathbf{x})$$

are unique. Therefore the equivariance condition (1.4) means, equivalently, that $\pi \mathbf{x}(t)$ is a solution of (1.5), whenever $\mathbf{x}(t)$ itself is a solution.

One example of group equivariant vector fields $\mathbf{f}(\mathbf{x})$ are the negative gradients

$$(1.6) \quad f_n(\mathbf{x}) := -\partial_n I(\mathbf{x})$$

of group invariants I . Here ∂_n denotes the partial derivative with respect to x_n , for $n = 1, \dots, N$.

The consequences of a *gradient structure* (1.6) are striking, even without any group invariance. Stationary solutions, alias equilibria $\mathbf{f}(\mathbf{x}) = 0$ of the ODE (1.5), become *critical points* $\nabla I(\mathbf{x}) = -\mathbf{f}(\mathbf{x}) = 0$. The *energy*, or *Lyapunov function*, $I(\mathbf{x}(t))$ decreases strictly with time t , along any nonstationary solution $\mathbf{x}(t)$. In particular, any solution $\mathbf{x}(t)$ which is bounded for all real times $-\infty < t < +\infty$ is *heteroclinic* between stationary solutions, i.e. $\mathbf{x}(t)$ becomes stationary for $t \rightarrow \pm\infty$. The energy I at the target equilibrium (or equilibria), for $t \rightarrow +\infty$, is always strictly lower than at the source, i.e. for $t \rightarrow -\infty$.

Note that the linear zero sum space

$$(1.7) \quad X_0 := \{\mathbf{x} \in X \mid p_1 := x_1 + \dots + x_N = 0\}$$

is an $(N - 1)$ -dimensional linear subspace of $X = \mathbb{R}^N$ which is invariant under the action (1.1) of S_N . The *standard representation* of S_N on X_0 is given by the restriction of the linear representation (1.1) to X_0 . That representation is *irreducible*: there does not exist any nontrivial proper subspace of X_0 which would also be invariant under all S_N .

The following cubic S_N -equivariant vector field, with arbitrary real parameters λ and c , is the main object of our present study

$$(1.8) \quad \dot{x}_n = f_n(\mathbf{x}) := (\lambda + c \cdot \langle x^2 \rangle) x_n + \widetilde{x}_n^2 + \widetilde{x}_n^3.$$

Here we use the abbreviations

$$(1.9) \quad \langle x^m \rangle := \frac{1}{N} p_m(\mathbf{x}), \quad \widetilde{x}_n^m := x_n^m - \langle x^m \rangle$$

for the averages and the offsets of m -th powers. It is a simple, but useful, exercise to check that the zero sum space X_0 is indeed invariant, not only under the linear action (1.1) of the group S_N but also under the nonlinear dynamics of (1.8). Indeed $\langle x \rangle = \langle \widetilde{x}_n^m \rangle = 0$.

It turns out that, up to scaling and possible time-reversal, the ODE (1.8) on X_0 represents the most general cubic vector field which is equivariant under the standard representation (1.1), (1.7); see [GoSt02], 2.4–2.7. A much more detailed source, which is difficult to obtain, is the thesis [Elm01].

To derive (1.8) from these results we first recall that *all* S_N -equivariant polynomial vector fields \mathbf{f} of the standard representation on X_0 , up to and including order three, are in fact gradients (1.6) of polynomial invariants I up to order four. In the notation (1.9), this provides the general form

$$(1.10) \quad \dot{x}_n = f_n(\mathbf{x}) = \lambda x_n + A \widetilde{x}_n^2 + B \widetilde{x}_n^3 + C \langle x^2 \rangle x_n$$

of (1.8). For $A, B \neq 0$, indeed, linear rescalings $t \rightarrow \tau t$, $x_n \rightarrow \sigma x_n$ amount to the replacements

$$(1.11) \quad \lambda \rightarrow \tau\lambda, \quad A \rightarrow \tau\sigma A, \quad B \rightarrow \tau\sigma^2 B, \quad C \rightarrow c := \tau\sigma^2 C.$$

Renaming $\tau\lambda$ as λ , the choices $\sigma = A/B$, $\tau = B/A^2$ then lead to (1.8) with

$$(1.12) \quad c := C/B.$$

Note that negative B , in particular, are associated with *time reversal* in (1.8).

The importance of the dynamics (1.8) reaches far beyond any direct interpretation as a network of N identical scalar “cells” with all-to-all coupling via power sums. Indeed, the bifurcation analysis of any fully permutation-symmetric network, at eigenvalue 0, typically leads to irreducible eigenspaces. Beyond total synchrony $x_1 = \dots = x_N$, the standard representation on X_0 provides the simplest interesting case. Any center manifold reduction, and subsequent truncation to cubic terms will then lead to our reference bifurcation problem (1.8) with one or the other value of the one remaining coefficient c . See section 7 for an explicit example.

In fact, the cubic case (1.8) possesses a *gradient structure* (1.6). Indeed, $f_n(\mathbf{x}) := -\partial_n I(\mathbf{x})$ holds on X_0 , as required in (1.6), with the quartic polynomial

$$(1.13) \quad -I(\mathbf{x}) := \left(\frac{1}{2}\lambda \cdot p_2 + \frac{1}{4N}c \cdot p_2^2\right) + \left(\frac{1}{3}p_3 - \frac{1}{N}p_1p_2\right) + \left(\frac{1}{4}p_4 - \frac{1}{N}p_1p_3\right).$$

Here we have used $p_1 = 0$ on X_0 .

Our main results on the bifurcation diagrams of (1.8), with respect to the bifurcation parameter λ , are presented and discussed in section 6. We distinguish seven zones of qualitatively different global heteroclinic dynamics. The diagrams are distinguished by seven parameter ranges for the cubic coefficient c .

The remaining sections are organized as follows.

In section 2 we study *3-cluster solutions*, i.e. solutions $\mathbf{x}(t)$ of our reference ODE (1.8) which feature at most three different values of the components x_n . More generally, an *M-cluster* features at most $M < N$ values

$$(1.14) \quad \{x_1, \dots, x_N\} = \{\xi_1, \dots, \xi_M\}.$$

Note how M -clusters degenerate to M' -clusters, for some $M' < M$, when some of the ξ -components still coincide.

As Kuramoto noticed long ago [NK95], all stationary solutions of (1.8) are (at most) 3-clusters. The reason is simple: any stationary component $\xi = \xi_k = x_n$ must satisfy the same cubic equation

$$(1.15) \quad 0 = f_n(\mathbf{x}) = \left(\lambda + c \cdot \frac{1}{N}p_2\right)\xi + \left(\xi^2 - \frac{1}{N}p_2\right) + \left(\xi^3 - \frac{1}{N}p_3\right),$$

with the same coefficients c, λ, p_2, p_3 . This admits at most three distinct cluster values $\xi = \xi_1, \xi_2, \xi_3$.

We aim at the dynamics of certain 3-cluster solutions which become heteroclinic between 2-cluster equilibria. In section 2 we simplify this task as follows. For $k = 1, 2, 3$, let N_k count the number of components n which satisfy $x_n = \xi_k$; note $N_1 + N_2 + N_3 = N$. We then pass to the limit $N \rightarrow \infty$ of large clusters $N_1 + N_3$ with a remaining *rebel cluster* N_2 of uniformly bounded size; for example we may fix $N_2 = 1$. Heteroclinic orbits between 2-cluster equilibria are then characterized by

$$(1.16) \quad \xi_2(t) - \xi_1(t) \rightarrow 0 \quad \text{or} \quad \xi_3(t) - \xi_2(t) \rightarrow 0,$$

for $t \rightarrow \pm\infty$.

In section 3 our heteroclinic objective gets simplified, in the limit $N = \infty$, by the somewhat surprising appearance of a skew product structure over the scalar quantity $s(t) := (\xi_3(t) - \xi_1(t))/(\alpha + 1)$. Here $\alpha := N_1/N_3$ denotes the relative population fraction of components in the large clusters. The gradient structure (1.13) leads to asymptotically stationary s_* ,

$$(1.17) \quad s(t) := (\xi_3(t) - \xi_1(t))/(\alpha + 1) \longrightarrow s_* = \text{const},$$

for $t \rightarrow \pm\infty$. See section 4 for a detailed analysis of this dynamics, which drives the skew product.

In section 5 we pass to the asymptotic states of stationary $s = s_* = \text{const}$. In suitable coordinates $y = \xi_2 - \xi_1$, this reduces our task to the discussion of a single scalar ODE

$$(1.18) \quad \dot{y} = y(y - (\alpha + 1)s_*)(y - \bar{y}(s_*))$$

on the real line; see (3.8), (5.2).

Rebel heteroclinic solutions between 2-clusters will easily be identified. Indeed, the 2-cluster stationary solutions $\xi_2 = \xi_1$ and $\xi_2 = \xi_3$ correspond to the stationary solutions $y = 0$ and $(\alpha + 1)s_*$, respectively. At the crucial 3-cluster equilibrium $\bar{y}(s_*)$, the small rebel cluster $\xi_2(t)$ might get stuck in its transition between the two major clusters ξ_1, ξ_3 . We call this phenomenon *blocking* of 2-cluster heteroclinicity.

We thus arrive at the alternative of 2-cluster heteroclinicity, versus blocking of heteroclinicity by a 3-cluster. The six critical parameters

$$(1.19) \quad c = -2, -\frac{3}{2}, -\frac{4}{3}, -\frac{5}{4}, -1, -\frac{1}{2}$$

mark transitions between qualitatively different bifurcation diagrams of our cubic reference equation (1.8). In section 6 we illustrate the resulting seven intermediate cases by diagrams of the stationary 2-clusters in a plane $(N_1/N, s)$; see figures 6.1–6.8.

Each diagram is foliated by the parameters λ , as level curves, where such stationary 2-clusters appear. A transversality assumption suggests the heteroclinic dynamics, in the non-blocking regions, to indicate a slow drift of the population fraction α , along constant parameter levels λ , by successive transitions of small rebel population fractions N_2 between the major clusters. Contrary to standard intuition, these rebel transitions do not always favor the larger cluster. The seven cases which we discuss in fact indicate

how cluster dynamics is an exceedingly subtle phenomenon, even in our simplistic cubic setting.

In section 7 we conclude with the promised application to clustering in Stuart-Landau oscillators with global complex linear coupling.

So, where are the theorems? The present paper is a rather detailed case study of S_N -equivariant 3-cluster dynamics in the standard representation on X_0 , as is. Our main focus is the rebel dynamics among the plethora of coexisting 2-cluster solutions of size ratios $\alpha = N_1/N_3$, for large N . One novelty is our unusual presentation of the heteroclinic rebel dynamics as a formal flow on the level set diagrams $\lambda = \lambda(\alpha, s)$, in section 5, where $s = (\xi_3 - \xi_1)/(\alpha + 1)$ measures asynchrony. All of section 6 can then be read as a long theorem, which establishes the pairwise inequivalence of these formal flows in the seven intervals

$$(1.20) \quad c \notin \left\{ -2, -\frac{3}{2}, -\frac{4}{3}, -\frac{5}{4}, -1, -\frac{1}{2} \right\}.$$

We conjecture, conversely, equivalence of the formal flows in each of the seven complementary intervals. Alas, we did not embark on the, more cumbersome than enlightening, proof of this somewhat academic question.

Acknowledgment. The first author gratefully acknowledges the deep inspiration by, and hospitality of, his coauthors at München who initiated this work. Ian Stewart personally provided us with a copy of the extensive thesis [Elm01], which saved us quite some duplication of effort. Extensive corrections of ever so many revisions were most diligently typeset by Patricia Habasescu. This work has also been supported by the Deutsche Forschungsgemeinschaft, SFB910, project A4 “Spatio-Temporal Patterns: Control, Delays, and Design”, and by KR1189/18 “Chimera States and Beyond”.

2 Cluster dynamics

Let $\dot{\mathbf{x}} = \mathbf{f}(\mathbf{x})$, on the zero sum space $\mathbf{x} \in X_0$, denote any vector field which is equivariant under the standard irreducible action of the symmetric group S_N on X_0 . See (1.1)–(1.5) and (1.7). The M -clusters are defined as those vectors $\mathbf{x} \in X_0$ which possess at most M distinct components x_n ; see (1.14). After applying a suitable permutation $\pi \in S_N$ to \mathbf{x} if necessary, we may assume without loss of generality that the indices are sorted as

$$(2.1) \quad x_1 = \dots = x_{N_1}, \quad \dots, \quad x_{N_1+\dots+N_{M-1}+1} = \dots = x_N.$$

We call N_k the *size* of cluster k , for $k = 1, \dots, M$. In other words, \mathbf{x} is fixed under the direct product $S_{\mathbf{N}} := S_{N_1} \times \dots \times S_{N_M}$ of permutation subgroups, where the first factor S_{N_1} acts on the first N_1 components of \mathbf{x} , and so on. Any other M -cluster is fixed under a group suitably conjugate to $S_{\mathbf{N}}$.

By (1.4), the linear space of $S_{\mathbf{N}}$ -fixed vectors x is invariant under the ODE flow of \mathbf{f} . In particular, nondegenerate M -clusters remain nondegenerate M -clusters, for all time. Only for $t \rightarrow \pm\infty$, an M -cluster $\mathbf{x}(t)$ may possibly limit onto an M' -cluster with fewer

clusters, i.e. $M' < M$. Since any stationary solutions are at most 3-clusters, by (1.15), this is precisely the situation which we plan to study, for $M = 3$ and $M' = 2$.

Specifically, consider the dynamics of any nondegenerate 3-cluster

$$(2.2) \quad \{x_1, \dots, x_n\} = \{\xi_1, \xi_2, \xi_3\}$$

in our reference ODE (1.8). Then the power sums p_m of (1.3) become

$$(2.3) \quad p_m = N_1 \xi_1^m + N_2 \xi_2^m + N_3 \xi_3^m.$$

The cluster sizes $N_k \geq 1$, respectively, count the number of times the distinct values ξ_k occur among the x_n .

With these weighted power sums p_m , the resulting dynamics of the ξ_k is of course given by the ODE

$$(2.4) \quad \dot{\xi}_k = (\lambda + c \cdot \frac{1}{N} p_2) \xi_k + (\xi_k^2 - \frac{1}{N} p_2) + (\xi_k^3 - \frac{1}{N} p_3),$$

for $k = 1, 2, 3$. Here we have simply replaced x_n by ξ_k , in (1.8).

Taking differences $\xi_j - \xi_k$ of any two equations in (2.4) we obtain

$$(2.5) \quad \frac{d}{dt}(\xi_j - \xi_k) = (\xi_j - \xi_k) \left(\lambda + c \cdot \frac{1}{N} p_2 + (\xi_j + \xi_k) + (\xi_j^2 + \xi_j \xi_k + \xi_k^2) \right).$$

We now introduce the redundant scaled difference variables

$$(2.6) \quad y_1 := \frac{N_3}{N}(\xi_2 - \xi_1), \quad y_2 := \frac{N_3}{N}(\xi_3 - \xi_2), \quad y_3 := \frac{N_3}{N}(\xi_1 - \xi_3) = -(y_1 + y_2).$$

The flow invariant zero sum space X_0 of (1.7) becomes planar, in the variables ξ_k :

$$(2.7) \quad 0 = p_1 = N_1 \xi_1 + N_2 \xi_2 + N_3 \xi_3.$$

Therefore it is not surprising that we can invert the transformation from the redundant coordinates (ξ_1, ξ_2, ξ_3) on X_0 to $(y_1, y_2) \in \mathbb{R}^2$ by

$$(2.8) \quad \begin{aligned} \xi_1 &= -(1 + \frac{N_2}{N_3})y_1 && -y_2; \\ \xi_2 &= \frac{N_1}{N_3}y_1 && -y_2; \\ \xi_3 &= \frac{N_1}{N_3}y_1 && +(\frac{N_1}{N_3} + \frac{N_2}{N_3})y_2. \end{aligned}$$

In principle, this allows us to rewrite the 3-system (2.4), i.e. a planar system on X_0 , in terms of the two new variables y_1, y_2 . Since the general expressions are a little messy we simplify this calculation for the limit $N \rightarrow \infty$ of large symmetric groups S_N , in the next section.

3 The limit of large symmetric groups S_N

As announced in the introduction, we now consider the S_N -equivariant 3-cluster dynamics (2.4) of (1.8), in the limit of large N . Specifically, we assume that the cluster size N_2 remains small compared to $N_1 + N_3 = N - N_2$, i.e.

$$(3.1) \quad N_2/N \rightarrow 0, \quad \text{for } N \rightarrow \infty.$$

We consider a fixed finite asymptotic size ratio

$$(3.2) \quad N_1/N_3 \rightarrow \alpha \in (0, \infty)$$

of the two large clusters sizes N_1 and N_3 , in the limit $N \rightarrow \infty$. Note how (3.1) is equivalent to $N_2/N_3 \rightarrow 0$, and likewise to $N_2/N_1 \rightarrow 0$, for $N \rightarrow \infty$. We therefore call the comparatively tiny cluster (N_2, ξ_2) the *rebel cluster*.

Inserting these limits into the transformation (2.8) above provides the simplified expressions

$$(3.3) \quad \begin{aligned} \xi_1 &= -y_1 & -y_2; \\ \xi_2 &= \alpha y_1 & -y_2; \\ \xi_3 &= \alpha y_1 & +\alpha y_2. \end{aligned}$$

In the above limit $N \rightarrow \infty$, this allows us to rewrite the 3-cluster ODE (2.4) in the still slightly unwieldy planar form

$$(3.4) \quad \dot{y}_1 = y_1 \left(\lambda + (\alpha - 1)y_1 - 2y_2 + (\alpha^2 - \alpha + 1)y_1^2 + 3(1 - \alpha)y_1y_2 + 3y_2^2 + \alpha c(y_1 + y_2)^2 \right)$$

$$(3.5) \quad \dot{y}_2 = y_2 \left(\lambda + 2\alpha y_1 + (\alpha - 1)y_2 + 3\alpha^2 y_1^2 + 3\alpha(\alpha - 1)y_1y_2 + (\alpha^2 - \alpha + 1)y_2^2 + \alpha c(y_1 + y_2)^2 \right)$$

Just for academic completeness – or so it seems at first – let us also write the resulting ODE for the sum

$$(3.6) \quad s := y_1 + y_2 = -y_3 = (\xi_3 - \xi_1)/(\alpha + 1)$$

which redundantly appears in (2.6):

$$(3.7) \quad \dot{s} = s \left(\lambda + (\alpha - 1)s + qs^2 \right); \quad q := \alpha^2 + (c - 1)\alpha + 1.$$

This is a scalar ODE for the sum s alone. In particular, bounded solutions $s(t)$ converge to some equilibria $s \equiv s_*$ of (3.7) for $t \rightarrow \pm\infty$, respectively. Substitution of $y_2 = s - y_1$ in (3.4) provides the complementing ODE

$$(3.8) \quad \dot{y}_1 = (\alpha + 1)^2 y_1 (y_1 - s) (y_1 - \bar{y}_1(s)) + y_1 \dot{s}/s.$$

Here we have abbreviated

$$(3.9) \quad \bar{y}_1(s) := (\alpha + 1)^{-1}((2 - \alpha)s - 1).$$

The polynomial \dot{s}/s abbreviates the quadratic parenthesis of (3.7).

In conclusion, we observe a *skew product structure*, in the limit $N \rightarrow \infty$ of two large clusters N_1, N_3 , and one comparatively small cluster N_2 . Indeed the two ODEs (3.7) and (3.8) identify the asymptotic 3-cluster dynamics (2.4) in the zero sum subspace X_0 of (2.7) as a system where the autonomous dynamics (3.7) of s drives the scalar dynamics (3.8) of y_1 .

Perhaps this structure of our restricted 3-cluster problem should not surprise us, after all. In fact, (3.7) describes the dynamics s of the two large clusters ξ_1, ξ_3 which is not affected by the comparatively small number N_2 of rebels ξ_2 . Ignoring N_2 , indeed, the zero sum condition (2.7) implies conservation of $N_1\xi_1 + N_3\xi_3 = 0$, and hence a one-dimensional autonomous dynamics for the difference variable $s = (\xi_3 - \xi_1)/(\alpha + 1)$ of (3.6). Because $s = 0$ indicates synchrony of the two large clusters, i.e. effectively a one-cluster dynamics, we also call s the *asynchrony variable*. The rebel dynamics (3.8) describes the remaining deviation $y_1 = (\xi_2 - \xi_1)/(\alpha + 1)$ of the rebels ξ_2 in the small cluster (N_2, ξ_2) from the state ξ_1 of the large cluster (N_1, ξ_1) , once the two large clusters $(N_1, \xi_1), (N_3, \xi_3)$ have reached a status quo equilibrium $s = s_*$ according to their size ratio $\alpha = N_1/N_3$.

4 Two-cluster dynamics

In this section we discuss the autonomous two-cluster dynamics. By (3.7), we only have to study the asynchrony sum $s = (\xi_3 - \xi_1)/(\alpha + 1) = y_1 + y_2$ defined in (3.6), i.e.

$$(4.1) \quad \dot{s} = s(\lambda + (\alpha - 1)s + qs^2) .$$

Here the asymptotic ratio $0 < \alpha = \lim N_1/N_3 < \infty$ of the sizes N_1 and N_3 of the two large clusters, for $N \rightarrow \infty$, is a fixed parameter, in addition to the cubic coefficient c and the bifurcation parameter λ . Also from (3.7), we recall the abbreviation

$$(4.2) \quad q = q(\alpha) := \alpha^2 + (c - 1)\alpha + 1$$

for the quadratic coefficient q .

The scalar ODE (4.1) is cubic in s with trivial equilibrium $s = 0$. The remaining equilibria $s = s_*$ are characterized by the vanishing quadratic parenthesis in (4.1) at bifurcation parameters λ , i.e. at parameters

$$(4.3) \quad \lambda = \lambda(\alpha, s) := s(1 - \alpha - qs) .$$

Explicit and elementary calculations reveal the standard bifurcation diagrams with respect to λ , for fixed parameters α and c . For example we obtain

$$(4.4) \quad \dot{s} = s(\lambda - s(1 - s)) \quad \text{at } \alpha = 0, \quad q = 1;$$

$$(4.5) \quad \dot{s} = s(\lambda + (c + 1)s^2) \quad \text{at } \alpha = 1, \quad q = c + 1 .$$

We discuss three cases depending on the sign of $c + 1$, below. See section 6 for many additional examples.

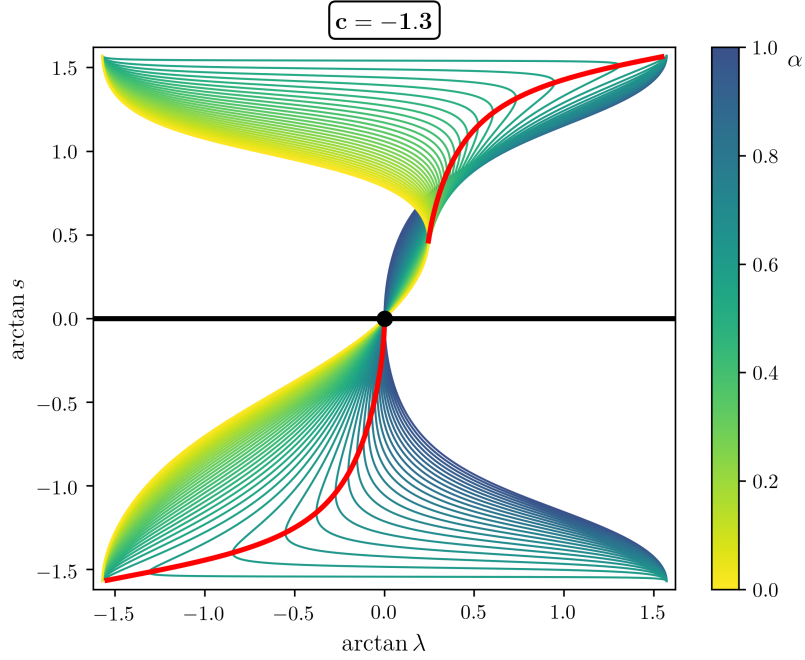


Figure 4.1: Global equilibrium bifurcation diagrams of the ODE flow (4.1) for the compactified asynchrony s defined in (3.6), with $c = -1.3 < -1$; see subsection 4.2. The compactified horizontal λ -axis (black) represents the one-cluster case of synchrony $s = 0$, for the large clusters. All 2-cluster bifurcation curves coexist, in the same phase space $\mathbf{x} \in X_0$, for realizable ratios $\alpha = N_1/N_3 \in [0, 1]$. The color shading indicates fixed values of α increasing from $\alpha = 0$ (yellow) to $\alpha = 1$ (blue), along each bifurcation curve in the (λ, s) plane. The quadratic coefficient q in (4.3) changes sign at $\alpha = \alpha_c \in (0, 1)$. The redundant cases $1/\alpha = N_3/N_1 \in (0, 1)$ are omitted. Red: the two branches of extreme saddle-node values of $(\lambda, s) = (\lambda_{\min\max}(\alpha), s_{\min\max}(\alpha))$ on each bifurcation curve; see (4.10),(4.11). Positive q , for $0 \leq \alpha < \alpha_c$, imply positive $s_{\min\max}$. Negative q , for $\alpha_c < \alpha \leq 1$, imply $s_{\min\max} < 0$. In-/stability of each stationary solution s_* can easily be derived from exchange of stability, at $\lambda = 0$ and the saddle-nodes, or explicitly from (4.1).

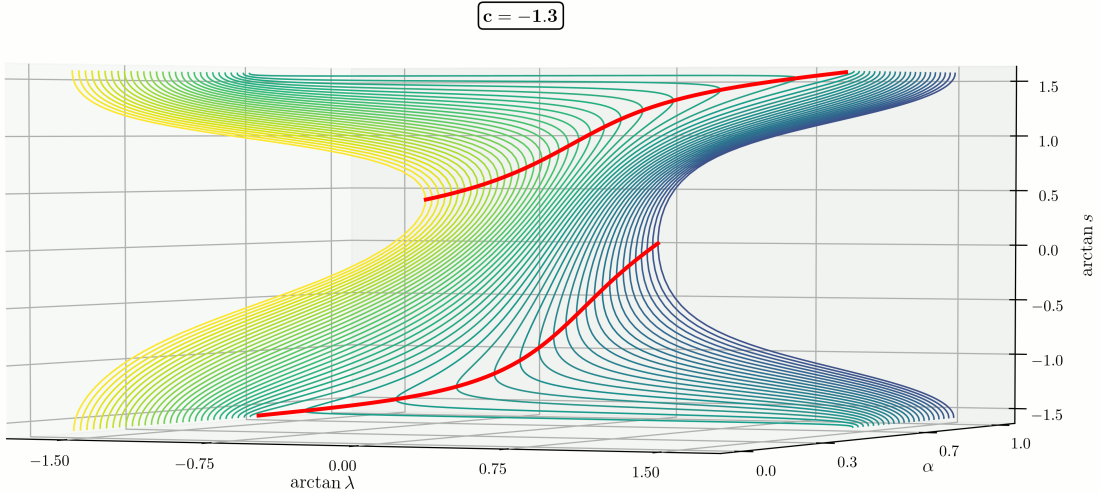


Figure 4.2: The bifurcation diagram of figure 4.1, rotated such that the cluster ratios $\alpha \in [0, 1]$ can be visualized as a second “parameter”. Color coding as before, but with yellow in front and blue in the background. Note the red fold curves, for the projection into the horizontal plane $(\arctan \lambda, \alpha)$.

4.1 The degenerate transition case $c = -1$

In this case, the quadratic coefficient $q = (\alpha - 1)^2$ is nonnegative and vanishes at $\alpha = 1$, only. Note how the s -dynamics becomes linear, $\dot{s} = \lambda s$, at $\alpha = 1$; see (4.5). For $0 \leq \alpha < 1$ we may rescale s to $\tilde{s} := (1 - \alpha)s$ and obtain the α independent ODE

$$(4.6) \quad \dot{\tilde{s}} = \tilde{s}(\lambda - \tilde{s} + \tilde{s}^2) .$$

which coincides with the case $\alpha = 0$ of (4.4).

Stability of the stationary solutions $s_* = \tilde{s}_*/(1 - \alpha)$ for any $0 \leq \alpha < 1$ is easily determined. For $\lambda < 1/4$, we have three stationary solutions \tilde{s}_* . Since

$$(4.7) \quad \dot{s} = qs^3 + \dots$$

with $q = (\alpha - 1)^2 > 0$, the top and bottom equilibrium are unstable, while the intermediate equilibrium is stable. At $\lambda = 1/4$, of course, we obtain a saddle-node equilibrium $s_* = \frac{1}{2}(1 - \alpha)^{-1}$. For $\lambda > 1/4$ only the trivial stationary solution $s_* = 0$ remains, which is unstable for all $\lambda > 0$.

4.2 The case $c < -1$

In this case, the quadratic coefficient $q = q(\alpha)$ in (4.1), (4.2) changes sign strictly, at

$$(4.8) \quad \alpha = \alpha_c := \frac{1}{2}(1 - c - \sqrt{(1 - c)^2 - 4}) \in (0, 1) .$$

Specifically $q > 0$, for $0 \leq \alpha < \alpha_c$, and $q < 0$, for $\alpha_c < \alpha \leq 1$. Interchanging N_1 with N_3 , we omit the redundant cases $\alpha = N_1/N_3 > 1$, at first.

For an example we fix the cubic coefficient $c = -1.3$. See figure 4.1 for the resulting bifurcation diagrams of (4.1). The nontrivial stationary solutions $s = s_*$ at fixed $\lambda = \lambda_*$ and size ratio $\alpha = \alpha_*$ appear as the intersections $s = s_*$ of the bifurcation curve for parameter α with the vertical line $\lambda = \lambda_*$, in this plot. The size ratio $\alpha = N_1/N_3$ may be considered as a fixed parameter, in any of the invariant cluster subspaces (2.1). We therefore plot the bifurcation diagrams as a family of curves, parametrized over discrete values α . Color coding is from yellow, at $\alpha = 0$, to blue, at $\alpha = 1$. Since all these bifurcation diagrams coexist, in the large $(N - 1)$ -dimensional phase space X_0 , we superimpose all bifurcation curves in figure 4.1.

The less standard contour plot of figure 4.3 tracks the level sets of the parameter $\lambda = \lambda(\alpha, s)$, as a function of $0 \leq \alpha = N_1/N_3 \leq 1$ (horizontal) and $-\pi/2 < \arctan s < \pi/2$ (vertical), at which nontrivial stationary solutions $s = s_*$ occur; see (4.3). We use $\arctan s$ again, rather than s itself, for compactification of the unbounded range of $s \in \mathbb{R}$. The level sets are in fact level curves because the only critical point \mathbf{F} of λ , located at $(N_1/N_3 = 1, s = 0)$, is a nondegenerate saddle. This accounts for the two level curves of $\lambda = 0$, one solid black and one dotted yellow, which intersect at \mathbf{F} . The third level curve of $\lambda = 0$ emanates from the left boundary as a dotted yellow curve.

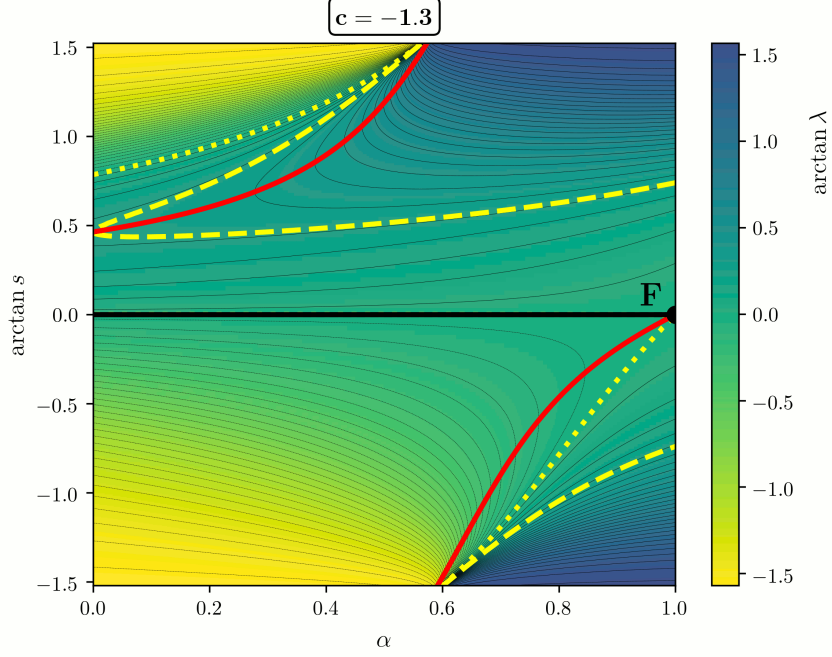


Figure 4.3: Level curves of $\lambda = \lambda(\alpha, s)$ for nontrivial stationary solutions $s = s_* > 0$ of the ODE flow (4.1) with $c = -1.3 < -1$. Here $\alpha = N_1/N_3$ is horizontal, and $\arctan s$ is plotted vertically. Colors from yellow to blue indicate increasing values of $-\infty < \lambda < +\infty$, this time. Note the black and the two dotted yellow level curves of $\lambda = 0$ which intersect at the only critical point **F** of $\lambda(\alpha, s)$. In particular, any level curve begins and terminates at the boundary, as described in the text. Another example is the dashed yellow level curve of the value $\lambda = 1/4$. Restricted to the left vertical s -axis, at $\alpha = 0$, this is the maximal value of λ . As in figure 4.1, the two red curves indicate the values $s = s_{\min\max}(\alpha)$ where saddle-node bifurcations occur at the levels $\lambda = \lambda_{\min\max}(\alpha)$. Equivalently, they indicate extremal values of α , on level curves of λ in that region. The region of stable equilibria $s = s_*$ is located between the two red curves.

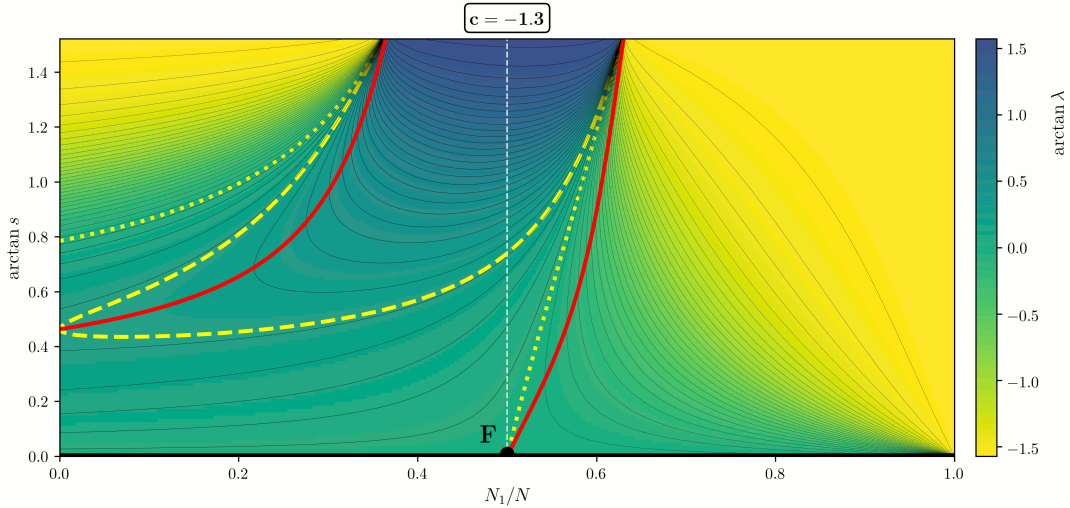


Figure 4.4: The substitution $N_1 \leftrightarrow N_3$, $y_1 \leftrightarrow -y_2$ allows for a gluing identification $s \leftrightarrow -s$ at the right boundary $\alpha = N_1/N_3 = 1$ of figure 4.3. The new horizontal axis $N_1/N = \alpha/(\alpha + 1) \in [0, 1]$ therefore compactifies cluster ratios $\alpha \in [0, \infty]$ and allows us to omit $s < 0$ as redundant. The break-even point $N_1/N = 1/2$, alias $\alpha = 1$, of equal cluster size $N_1 = N_3$ is marked by a vertical dashed white line. Again, the region of stable equilibria $s = s_*$ is located between the two red curves.

Next we drop the assumption $\alpha = N_1/N_3 \leq 1$ and allow arbitrary sizes N_1, N_3 of the two clusters. Without loss of generality, we may then label the large clusters (N_1, ξ_1) and (N_3, ξ_3) such that the asynchrony

$$(4.9) \quad s = (\xi_3 - \xi_1)/(\alpha + 1) > 0$$

is strictly positive. This allows us to discard the redundantly symmetric case $s < 0$, a priori. Caution is required because our choice admits any cluster ratio $\alpha = N_1/N_3 \in (0, \infty)$. To represent α , we therefore use the percentage $N_1/N = \alpha/(\alpha + 1) \in [0, 1]$ as a compactification of the horizontal axis, in figure 4.4 and all subsequent level plots of the same style. The important break-even point $\alpha = N_1/N_3 = 1$ of equal cluster parity $N_1 = N_3$, alias $N_1/N = 1/2$, is marked by a thin white vertical line.

Each level curve of $\lambda(\alpha, s) = \lambda$ terminates at two points on the boundary of figure 4.3. Any termination at the upper or lower boundary $s = \pm\infty$ must occur at $\alpha = \alpha_c$, where $q = 0$. Indeed, $\lambda = -qs^2 + \dots$ in (4.3) implies limits $\lambda = -(\text{sign } q) \cdot \infty$, for $s = \pm\infty$ and $q \neq 0$. At the left and right boundaries $\alpha = 0$ and $\alpha = 1$ we encounter the values $\lambda(0, s) = s(1 - s)$ and $\lambda(1, s) = -(c + 1)s^2$, respectively. See (4.4), (4.5).

Along each level curve $\lambda(\alpha, s) = \lambda_*$, we may also determine the local extrema of α , i.e. the vertical tangents of the level curves. Equivalently, these are the local extrema of $\lambda(\alpha, s)$, for any fixed $\alpha = \alpha_*$. An elementary calculation shows that these curves are given by the level sets of $0 = \partial_s \lambda(\alpha, s) = 1 - \alpha - 2qs$, i.e.

$$(4.10) \quad s = s_{\min\max}(\alpha) := \frac{1}{2}(1 - \alpha)/q > 0,$$

$$(4.11) \quad \lambda = \lambda_{\min\max}(\alpha) := \lambda(\alpha, s_{\min\max}(\alpha)) = \frac{1}{4}(1 - \alpha)^2/q.$$

These locations are marked in figures 4.1, 4.3, 4.4 as two red curves. Comparing (4.3) and (4.10), the red curves of saddle-nodes occur at half the s -value of the nontrivial dotted yellow level curve $\lambda = 0$, for each α .

In-/stability of each stationary solution $s = s_*$ can be derived easily from exchange of stability, at $\lambda = 0$, or explicitly from (4.1). As in the previous subsection 4.1, positive $q = q(\alpha) > 0$ implies instability of the largest and smallest equilibria s_* , and stability of any intermediate s_* , on each level curve λ and for each fixed α . This identifies the region of s between the two red saddle-node curves $s = s_{\min\max}(\alpha)$ as the only region of stable stationary solutions $s = s_*$. We call such regions of α, s_* where the equilibrium $s \equiv s_*$ is stable an *s-stable region*. The *s-unstable region* consists of the two parts below and above the two red saddle-node curves.

Negative sign $q(\alpha, c) < 0$ in contrast, which only occurs for $\alpha_c \leq \alpha \leq 1/\alpha_c$, indicates stability of the largest and smallest equilibria $s = s_*$, and instability of any intermediate s_* , there. In particular, this also identifies $\alpha_c < \alpha < 1/\alpha_c$ as the region where the dynamics of 4.1 is *dissipative*, i.e. where solutions $s(t)$ are attracted to a bounded region in forward time.

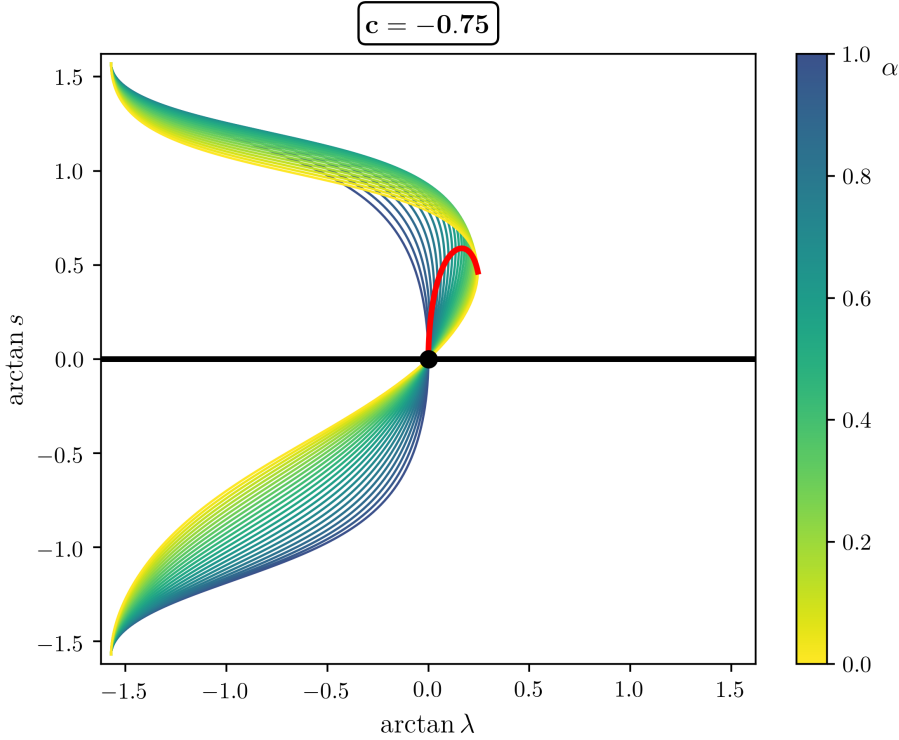


Figure 4.5: Bifurcation diagrams of the ODE flow (4.1) for the asynchrony s defined in (3.6) at $c = -0.75 > -1$; see subsection 4.3. The quadratic coefficient q remains positive for all $0 \leq \alpha \leq 1$. See figure 4.1 for colors and in-/stability of each stationary solution s_* . Note the single red branch of saddle-nodes at extremals $\lambda = \lambda_{\min\max}(\alpha)$, according to (4.10),(4.11). Indeed $q > 0$ implies $\lambda_{\min\max} > 0$ and $s_{\min\max} > 0$.

4.3 The case $c > -1$

In this case, the quadratic coefficient $q = q(\alpha)$ in (4.1), (4.2) is strictly positive, for all $0 < \alpha < \infty$. Therefore our discussion follows the part of the previous subsection 4.2 for the case $q > 0$. For an explicit example we fix the cubic coefficient $c = -0.75$. See figure 4.5 for the resulting bifurcation diagrams of (4.1).

In the less standard contour plots of figures 4.6, 4.7, analogously to figures 4.3, 4.4, we present the level curves of the parameter $\lambda = \lambda(\alpha, s)$. The only critical point of λ is still the nondegenerate saddle \mathbf{F} , with two associated level curves $\lambda = 0$ (solid black and dotted yellow). This time, $-\infty < \lambda \leq 1/4$ is bounded above, globally, as is already visible from the bifurcation diagrams of figure 4.5. The maximal λ is attained on the left boundary $\alpha = 0$, at $s = 1/2$.

Each level curve terminates at two points on the boundary of figures 4.6, 4.7, as before. Since $\lambda = -\infty$ at $s = +\infty$, this time, all terminations occur at the right and left boundaries. In the left region, delimited by the black and yellow level curves of $\lambda = 0$, both terminations are located on the left boundary. The maximal value of α , along each of the interior level curves of $0 < \lambda < 1/4$, occurs on the red curve of saddle-nodes, of course. Again that red curve is located at half the s -value of the dotted yellow level

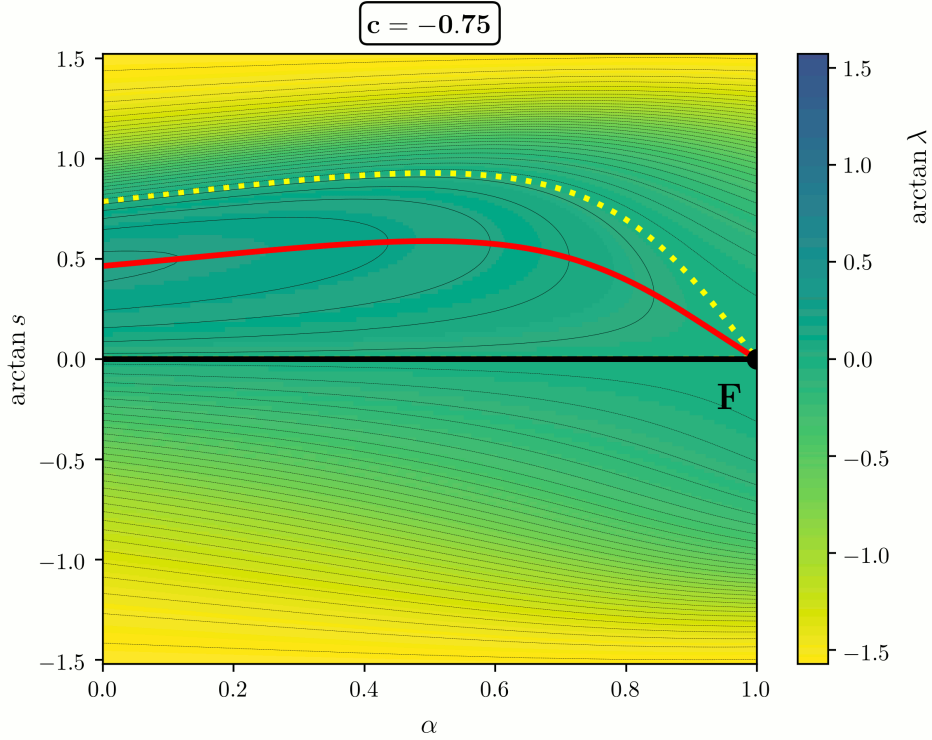


Figure 4.6: Level curves of $\lambda = \lambda(\alpha, s)$ for nontrivial stationary solutions $s = s_* > 0$ of the ODE flow (4.1) with $c = -0.75 > -1$, in analogy to the case $c = -1.3$ of figure 4.3. See the legend there. Note that $-\infty < \lambda \leq 1/4$ is now bounded above. There are only two level curves for $\lambda = 0$, one black and one dotted yellow. Again they intersect at the only critical point \mathbf{F} of $\lambda(\alpha, s)$. The maximal values of α , on level curves of λ , form a single red curve of saddle-node bifurcations, this time. See also figure 4.5. All level curves of λ still begin and terminate at the boundary, as described in the text. The region of stable equilibria $s = s_*$ is located between the black horizontal axis and the red saddle-node curve.

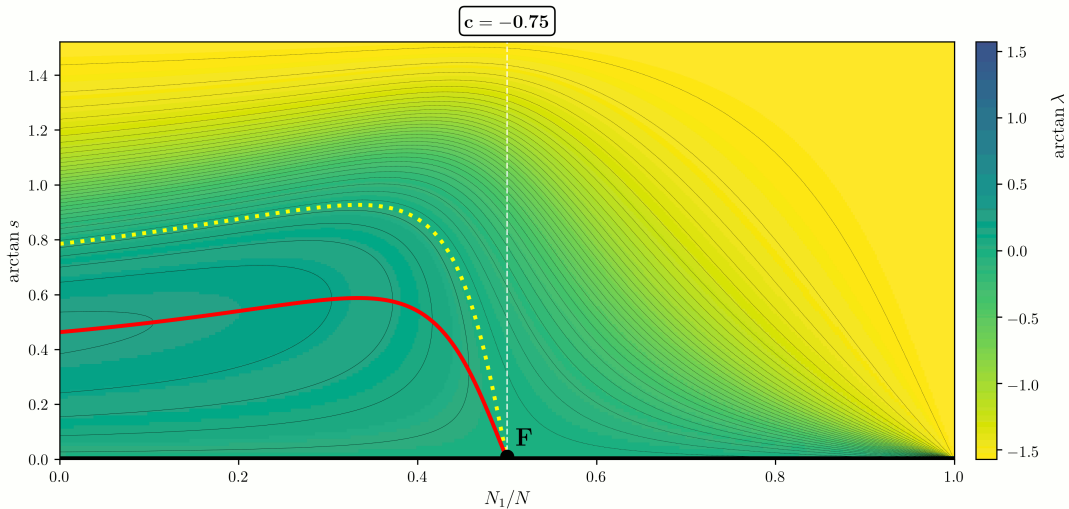


Figure 4.7: Glued version of figure 4.6. The horizontal axis is $N_1/N = \alpha/(\alpha + 1)$, and $s < 0$ has been omitted as redundant, analogously to the derivation of figure 4.4 from figure 4.3. The only stability region of nontrivial equilibria $s = s_* > 0$ is still confined between the black horizontal α -axis $s = 0$, and the red saddle-node curve $s = s_{\text{minimax}}(\alpha)$.

curve $\lambda = 0$, for each α . Above the region delimited by the dotted yellow curve $\lambda = 0$, in figure 4.7, level curves connect the two vertical boundaries $\alpha = 0$ and $\alpha = \infty$.

In-/stability of each stationary solution $s = s_* > 0$ can be derived easily, as before. Because $q > 0$, the region of s between the black horizontal α -axis and the red saddle-node curve $s = s_{\min\max}(\alpha)$ is the only s -stable region, for any $0 < \alpha < \infty$.

5 Rebel dynamics and blocking

We address the remaining ODE for $y := \xi_2 - \xi_1 = (\alpha + 1)y_1$ next; see (2.6), (3.8). In the previous section we have seen how the asynchrony variable $s = (\xi_3 - \xi_1)/(\alpha + 1)$ tends to total 1-cluster synchrony $s \equiv 0$ of the two large clusters, or to a nontrivial equilibrium $s \equiv s_* \neq 0$, for $t \rightarrow \infty$, where the two large clusters (N_1, ξ_1) and (N_3, ξ_3) compete for the rebels ξ_2 in size. In the present section, we study that remaining rebel dynamics of (N_2, ξ_2) , when the two large clusters have already equilibrated.

The synchrony case $s \equiv 0$ of large clusters leads to

$$(5.1) \quad \dot{y} = y(\lambda + y + y^2)$$

for $y = (\alpha + 1)y_1$. To derive (5.1) we directly replace $y_2 = s - y_1 = -y_1$ in (3.4), or we formally replace \dot{s}/s by λ in (3.8) due to (3.7).

For $\lambda > 1/4$, we obtain global instability of the fully synchronous 1-cluster equilibrium $0 \equiv s = (\xi_3 - \xi_1)/(\alpha + 1)$ towards rebels $y = \xi_2 - \xi_1$, which escape to $\pm\infty$. For $0 \neq \lambda < 1/4$, in contrast, we obtain a unique stable equilibrium $y \equiv y_*$. The domain of attraction is delimited by the remaining two linearly unstable equilibria, beyond which rebels y escape to $\pm\infty$, respectively, as before. Only for $\lambda < 0$ we have stability of $y_* = 0$ against rebellion, in this sense. For $0 < \lambda < 1/4$, where $0 > y_* > -1/2$, rebellion can lead to the gradual formation of a tiny stable rebel cluster at $y_* = -\frac{1}{2}(1 - \sqrt{1 - 4\lambda})$, at least as long as its tiny size N_2 remains small compared to $N \approx N_1 + N_3$. Also note the presence of a linearly unstable rebel cluster at $y \equiv -\frac{1}{2}(1 + \sqrt{1 - 4\lambda})$, for all $\lambda < 1/4$.

The 2-cluster case $s \equiv s_* \neq 0$, where the two large clusters compete for the rebels (N_2, ξ_2) , is much more interesting. From (4.9) we recall $s > 0$, without loss of generality.

Scaling (3.8), (3.9) to $y := (\alpha + 1)y_1 = \xi_2 - \xi_1$ again, we obtain the cubic ODE

$$(5.2) \quad \dot{y} = y(y - (\alpha + 1)s)(y - \bar{y}(s)),$$

$$(5.3) \quad \bar{y}(s) := (2 - \alpha)s - 1.$$

We repeat that $s \equiv s_* > 0$ is constant here. In particular, the term \dot{s}/s from (3.8) drops out in (5.2). The equilibrium $y = 0$ indicates $\xi_2 = \xi_1$: the rebels ξ_2 are at the cluster (N_1, ξ_1) . The equilibrium $y_1 = s$, i.e. $y = (\alpha + 1)s$, in contrast, indicates $\xi_2 = \xi_3$: the rebels are with the other cluster (N_3, ξ_3) . Indeed, $y_1 = s$ is equivalent to $y_2 = 0$, by (3.6), and hence to $\xi_2 = \xi_3$, by (2.6). The third equilibrium $y = \bar{y}(s)$ denotes a 3-cluster equilibrium where, in general, the tiny rebel cluster achieves its own equilibrium balance, holding out against both large clusters.

Suppose a nonstationary solution $y = y(t)$ of the scalar ODE (5.2) remains bounded for all positive and negative times $t \in \mathbb{R}$. Then $y(t)$ is heteroclinic. Consider a heteroclinic orbit of (5.2) from $y = 0$ to $y = (\alpha + 1)s$, as t increases from $t = -\infty$ to $t = +\infty$. This means that rebels leave the cluster (N_1, ξ_1) in favor of the cluster (N_3, ξ_3) . The discrete-valued parameter $\alpha = N_1/N_3$, along with $N_1/N = \alpha/(\alpha + 1)$, becomes continuous and real-valued in our asymptotics of large $N \rightarrow \infty$. Even though $\alpha = N_1/N_3$ is actually constant, we indicate the above rebel migration by a magenta arrow towards smaller N_1/N , along the level curves of constant λ , in figures 5.2– 5.5 further below.

In the opposite direction, a heteroclinic orbit of (5.2) from $y = (\alpha + 1)s$ to $y = 0$ indicates how rebels leave the cluster (N_3, ξ_3) in favor of the cluster (N_1, ξ_1) . We indicate this migration in favor of N_1 by an arrow towards larger N_1/N , in figures 5.3 and 5.5.

The arrows on level curves of λ carry meaning beyond the merely formal level. For large $N < \infty$, each such heteroclinic orbit amounts to a discrete step in the rational value of $\alpha = N_1/N_3$.

We illustrate this fundamental observation by numerical integration of Eq. (1.8) for $c = -1.3$, $\lambda = 0.18$ and $N = 32$ units. As initial condition, a two cluster solution $x_1 = \dots = x_{N_1} = \xi_1$, $x_{N_1+1} = \dots = x_N = \xi_3$ was chosen, with ξ_1 and ξ_3 as in section 3. For $N_1 = 4$, initially, this corresponds to an initial 2-cluster proportion of $N_1/N = 0.125$. We then perturb a single unit x_n , $n = N_1 + 1$, in cluster ξ_3 , and integrate forward in time until the dynamics no longer changes. As a result, we observe heteroclinic rebel dynamics, that is, the perturbed unit x_n changes its cluster affiliation from ξ_3 to ξ_1 . In other words, $N_1 = 5$, after the rebel transient. In Fig. 5.1 we repeat this process, for ever increasing cluster sizes N_1 . Note the successive heteroclinic transients of the rebels x_n , from ξ_3 down to $\xi_1 < \xi_3$. After 12 transients, of course, equal cluster parity $N_1 = N_2 = 16$ is reached. After 15 transients, the dynamics enters a blocking region and finally settles on a three cluster solution; see the bottom right part of Fig. 5.1. At this stage, the third coexisting cluster at $\xi_2 < \xi_3$ near $\xi_1 < \xi_2$ consists of just one single rebel element. This trajectory is also visualized in the $(N_1/N, s)$ plane of Fig. 5.2, with the color coding corresponding to the rebel cluster color in Fig. 5.1.

For numerical integration, we employed the implicit Adams method provided by SciPy; see [VG&al]. After each perturbation, we subtracted the mean of the ensemble to ensure the constraint $p_1 = 0$ in the phase space X_0 of (1.8). Note that by choosing initial conditions in the 2-cluster subspace with just a single unit perturbed, we suppress transitions in which multiple units might change their cluster affiliation, and instabilities that might break up the clusters altogether.

The direction of the heteroclinic transients partially determines the ordering, by decreasing energy or Lyapunov function $I(x)$ of (1.13), of the two asymptotic large 2-clusters. This would require a nontrivial calculation, otherwise. The transitivity of that order, simply following the level curves of λ along our arrows, possesses a dynamic counterpart. Assuming transversality of the stable and unstable manifolds of the target and source stationary cluster solutions, respectively, along heteroclinic orbits, there also exists a direct heteroclinic connection between any two equilibria connected by a directed

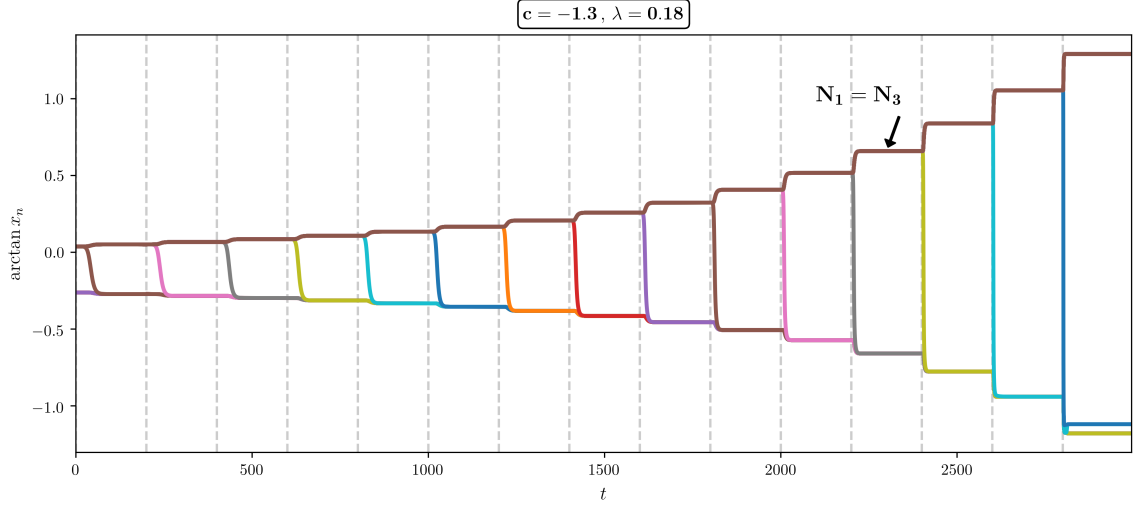


Figure 5.1: Trajectories obtained from numerical simulations of Eq. (1.8) for $c = -1.3$, $\lambda = 0.18$ and $N = 32$ units. We consider 2-cluster solutions $x_1 = \dots = x_{N_1} = \xi_1$, $x_{N_1+1} = \dots = x_N = \xi_3$ with ξ_1 and ξ_3 as in section 3. Starting from $N_1 = 4$ and $n = N_1 + 1$, we apply a small random perturbation to $x_n = \xi_3$ at a time indicated by the dashed vertical lines. We then integrate the system with rebel $x_n \neq \xi_1, \xi_3$, until the dynamics settles again. See the colored rebel transients of x_n from ξ_3 (top) to ξ_1 (bottom), along which the rebel x_n changes its cluster affiliation. We repeat this process until the system enters a blocking region because a stationary 3-cluster state is initiated by the rebel at $x_n = \xi_2$ (blue) between ξ_1 and ξ_3 ; see the last state shown in the figure.

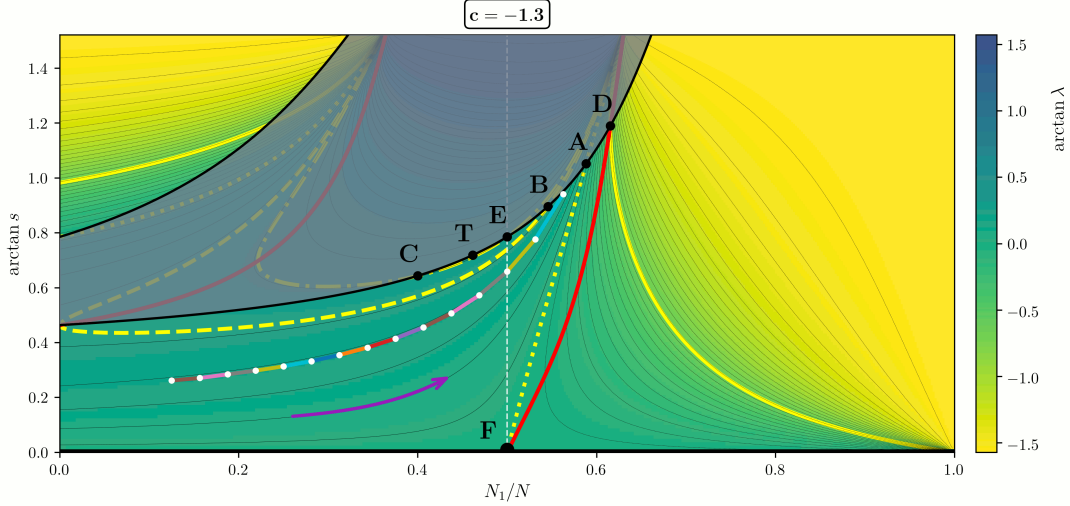


Figure 5.2: The rebel transients of figure 5.1 are inserted into the diagram of λ -levels from figure 4.4, within the level curve of $\lambda = 0.18$. The color coding of the rebel transients is the same as above. A magenta arrow indicates the drift direction of N_1/N , induced by the heteroclinic rebel transients. For further discussion of the yellow curves, and of the dark shaded blocking region where stationary rebel 3-clusters bifurcate and persist, we refer to figure 5.3 below.

sequence of heteroclinic orbits, for the same parameter λ . This *dynamic transitivity* is a consequence of the so-called λ -Lemma; see for example [PadM82]. The useful property of transversality of invariant manifolds, often called the Morse or Morse-Smale property, is generic for general vector fields, by the Kupka-Smale theorem. For our much more restrictive class of equivariant vector fields (1.8), however, transversality is a much more delicate assumption – somewhat beyond the scope of our present paper.

Heteroclinic orbits between $y = 0$ and $y = (\alpha + 1)s$ are blocked when the third rebel equilibrium $y = \bar{y}(s)$ of (5.2) is located strictly between $y = 0$ and $y = (\alpha + 1)s$. Therefore we call the equilibrium $\bar{y}(s)$ in (5.2), (5.3) *blocking*, if $0 < \bar{y}(s) < (\alpha + 1)s$. The *blocking regions*, in contour plots 5.2–5.5, consist of those $(N_1/N, s)$ for which the equilibrium $\bar{y}(s)$ blocks rebel heteroclinic orbits between the two large competing clusters. Instead the rebels are ready to form a tiny third cluster between the large ones, which may turn out stable, destabilizing the larger competitors, or unstable, stabilizing the 2-cluster status quo.

The *blocking boundaries* of the blocking region are characterized by those values of (α, s) for which $\bar{y}(s) = 0$ or $\bar{y}(s) = (\alpha + 1)s$, respectively. For the blocking boundary $\bar{y}(s) = 0$ we obtain the graphs

$$(5.4) \quad s = s_0(\alpha) := \frac{1}{2 - \alpha} > 0,$$

$$(5.5) \quad \lambda = \lambda_0(\alpha) := \frac{1 - (c + 2)\alpha}{(2 - \alpha)^2}.$$

Indeed (5.5) follows from (5.4) and (4.3). The blocking boundary $\bar{y}(s) = (\alpha + 1)s$ is analogously characterized by

$$(5.6) \quad s = s_1(\alpha) := \frac{1}{1 - 2\alpha} > 0,$$

$$(5.7) \quad \lambda = \lambda_1(\alpha) := \alpha \frac{\alpha - (c + 2)}{(1 - 2\alpha)^2}.$$

See figures 5.2–5.5, where we have added the two blocking boundaries as solid black curves to the corresponding previous plots 4.4, 4.7 for $c = -1.3, -0.75$. The blocking boundaries are easily distinguished by their values at $\alpha = 0$: $s_0 = 1/2$, $\lambda_0 = 1/4$ versus $s_1 = 1$, $\lambda_1 = 0$. Also note the poles at $\alpha = 2$, $N_1/N = 2/3$ and at $\alpha = 1/2$, $N_1/N = 1/3$, respectively.

It is remarkable that the rebel dynamics (5.2) does not depend on the cubic coefficient c , at all. In particular the blocking regions in the (α, s) -plane, and their black boundaries (5.4), (5.6), coincide in figures 5.2–5.5. Any differences arise from the configuration of level curves $\lambda = \lambda(\alpha, s)$, which certainly depend on c via (4.3); see also (5.5) and (5.7).

We determine the blocking regions and the direction of heteroclinic rebel dynamics in (5.2) next. Off the black blocking boundaries (5.4), (5.6), we sort the three stationary solutions $y = 0$, $(\alpha + 1)s$, $\bar{y}(s)$ as $\eta_1 < \eta_2 < \eta_3$, i.e.

$$(5.8) \quad \{0, (\alpha + 1)s, \bar{y}(s)\} = \{\eta_1, \eta_2, \eta_3\}.$$

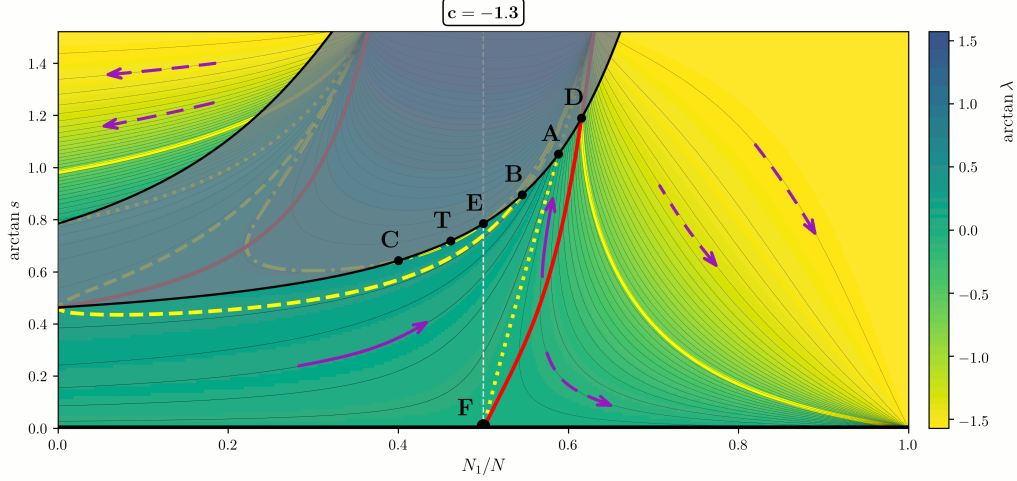


Figure 5.3: Level curves of $\lambda = \lambda(\alpha, s)$ for nontrivial stationary solutions $s = s_* > 0$ of the ODE flow (4.1) with $c = -1.3 < -1$, in coordinates $(N_1/N, \arctan s)$. See figure 4.4 for axes and color codings. The two solid black curves mark the boundaries of the blocking region. The new dotdashed yellow curve between **C** and **E** marks the level $\lambda = \lambda(\mathbf{E}) = -(c + 1)$. See figure 5.4 for a zoom into that region and a discussion of the tangency point **T**. The dashed yellow curve $\lambda = 1/4$ indicates the λ -level where one solid black blocking boundary terminates at $N_1/N = 0$. The other solid black blocking boundary left terminates at the level $\lambda = 0$ indicated by the previous dotted yellow curve. The blocking region is located between the two solid black boundaries and is indicated by a darker shading. Outside the shaded blocking region, magenta arrows along the level curves of $\lambda = \lambda(\alpha, s)$ to the right, i.e. towards larger cluster fractions N_1/N_3 , indicate heteroclinic rebel orbits from the cluster N_3 to the cluster N_1 . Similarly, magenta arrows to the left, i.e. towards smaller fractions N_1/N , indicate heteroclinic rebel orbits in the opposite direction, favoring the cluster N_3 . Note how directions change across the blocking region and across the red saddle-node curves. Magenta arrows are drawn solid, in the s -stable region, and are drawn dashed in the s -unstable region; see also figures 4.4 and 4.7. In the s -stable region, for example, rebellions from N_3 to any $N_1 < N_3$ will cause N_1 to grow beyond equal parity $N_1 = N_3$, across the white line $N_1/N = 1/2$ between **E** and **F**: from minority to majority. Growth of N_1 only terminates at the solid black blocking boundary, between **A** and **B**. See text for further details.

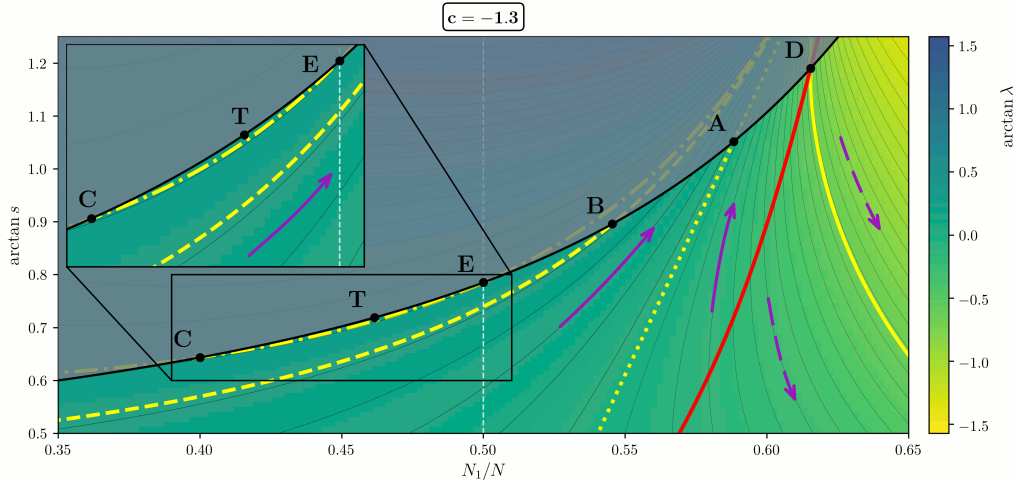


Figure 5.4: Zoom of figure 5.3. Note the tangency point **T**, further enlarged in the insert. Level curves of λ are tangent to the blocking boundary at **T**, from inside the dark shaded blocking region. In particular, level curves which emanate from the blocking boundary, between **C** and **T**, terminate on the blocking boundary, between the break-even point **E** and the tangency point **T**.

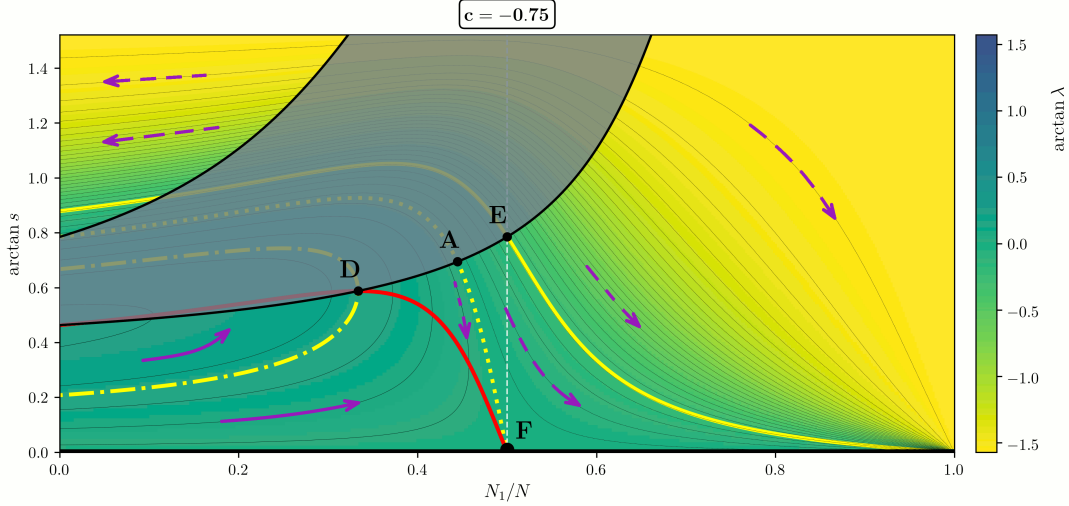


Figure 5.5: Level curves of $\lambda = \lambda(\alpha, s)$ as in figure 5.3, but for $c = -0.75 > -1$. The basic locations of the s -stable and the shaded y -blocking regions look similar, at first sight, but there are subtle differences in detail. See text.

Then $\dot{y} = (y - \eta_1)(y - \eta_2)(y - \eta_3)$ implies instability of the smallest and largest equilibria $y = \eta_1, \eta_3$, and stability of the intermediate equilibrium $y = \eta_2$. The two heteroclinic orbits run from η_1 and η_3 to η_2 , respectively.

For $s > 0$, i.e. $0 < (\alpha + 1)s$, this leaves us with the following three cases for the third equilibrium $\bar{y}(s)$.

Region 1: $\bar{y}(s) = \eta_1$.

This case is equivalent to $(2 - \alpha)s - 1 = \bar{y}(s) = \eta_1 < 0 = \eta_2 < \eta_3 = (\alpha + 1)s$, i.e. $s > 0$ is between the horizontal axis and the lower solid black blocking curve s_0 of (5.4). Then blocking does not occur, and heteroclinic rebel migration $y = \xi_2 - \xi_1$ runs from $y = (\alpha + 1)s = \eta_3$ down to $y = 0 = \eta_2$, i.e. from the cluster (N_3, ξ_3) towards the cluster (N_1, ξ_1) . We indicate this migration by a *magenta arrow towards larger α and N_1/N* , in figures 5.3– 5.5.

Region 2 (blocking): $\bar{y}(s) = \eta_2$.

Then $\eta_1 = 0 < \bar{y}(s) = (2 - \alpha)s - 1 = \eta_2 < \eta_3 = (\alpha + 1)s$, i.e. s is between the two black blocking curves. Blocking occurs, and heteroclinic rebel migration from either large cluster gets stuck at the intermediate equilibrium $y = \bar{y}(s) = \eta_2$. The resulting tiny new stationary rebel cluster at that 3-cluster equilibrium may in fact grow, at the expense of both large clusters, and with *indefinite effects on their proportion α* . Figures 5.2–5.5 indicate this blocking region by a darker shading.

Region 3: $\bar{y}(s) = \eta_3$.

Then $(2 - \alpha)s - 1 = \bar{y}(s) = \eta_3 > \eta_2 = (\alpha + 1)s > \eta_1 = 0$, i.e. s is above the upper red curve, and hence $0 \leq \alpha < 1/2$, $0 \leq N_1/N < 1/3$. Blocking does not occur, and heteroclinic rebel migration runs from $y = 0 = \eta_1$ upwards to $y = (\alpha + 1)s = \eta_2$, i.e. from the smaller cluster (N_1, ξ_1) towards the larger cluster

(N_3, ξ_3) : from minority to majority. We indicate this migration by a *magenta arrow towards smaller α* , in figures 5.3 and 5.5.

For example consider the s -stable region in figure 5.3, i.e. for $c = -1.3$. The region is located in the wedge between the lower black blocking boundary s_0 and the right red saddle-node curve. All level curves of $\lambda = \lambda(\alpha, s)$ in that region are oriented, along the solid magenta arrows, towards their termination at the black blocking boundary s_0 to the left of **D**. Rebel heteroclinic migration towards the cluster N_1 erodes the cluster N_3 , until eventual termination of the 2-cluster regime at the blocking boundary s_0 .

In fact, consider the s -stable 2-cluster states, which start out below the dashed yellow level curve $\lambda = 1/4$ from a minority cluster $N_1 < N_3$, i.e. from the left of the white line $N_1/N = \frac{1}{2}$ of equal parity $N_1 = N_3$. All these initial conditions will be prone to heteroclinic rebellion from the cluster N_3 to N_1 , across the white line and well into the region $N_1 > N_3$: from minority to majority, across equal cluster size.

In figure 5.5 in contrast, at $c = -0.75$, the red saddle-node boundary confines the s -stable subregion of region 1 to the left of the white line $N_1/N = \frac{1}{2}$, i.e. to $N_1 < N_3$. Therefore heteroclinic rebel orbits starting in the s -stable region cannot achieve equal parity, anymore. Instead, they face one of two possibilities:

- a) termination by blocking at the black blocking curve s_0 , or
- b) termination at the red saddle-node curve.

Migration from the larger cluster N_3 to N_1 gets stuck by an emerging tiny third rebel cluster, in case (a). The blocking 3-cluster equilibrium $y = \bar{y}(s) \gtrsim 0$ emerges near the smaller cluster $y = 0$, across the black blocking boundary $s = s_0(\alpha)$. In case (b), any further increase of N_1 stops at some status quo uneven 2-cluster with $N_1 < N_3$. The cause is the saddle-node termination of the 2-cluster. Indeed, the value of $\alpha = N_1/N_3$ at the saddle-node intersection is the maximal available value of α for any stationary 2-cluster, at that particular level of λ .

For later reference we also determine the regions of the cubic parameter c for which the black blocking boundaries $s = s_0(\alpha)$ and $s = s_1(\alpha)$, respectively, intersect with specific relevant dotted or dashed level curves of λ , or with the red saddle-node curves $s = s_{\min\max}(\alpha)$.

Specifically we claim the following four intersection points **A–D** of the lower black blocking boundary $s_0(\alpha) = 1/(2 - \alpha)$:

$$(5.9) \quad \mathbf{A} := s_0 \cap \{\lambda = 0\}, \quad 0 < \alpha < 2 \quad \iff \quad -\frac{3}{2} < c < +\infty;$$

$$(5.10) \quad \mathbf{B} := s_0 \cap \{\lambda = \frac{1}{4}\}, \quad 0 < \alpha < 2 \quad \iff \quad -\frac{3}{2} < c < -1;$$

$$(5.11) \quad \mathbf{C} := s_0 \cap \{\lambda = -(c + 1)\}, \quad 0 < \alpha < 2 \quad \iff \quad -\frac{3}{2} < c < -\frac{5}{4};$$

$$(5.12) \quad \mathbf{D} := s_0 \cap s_{\min\max}, \quad 0 < \alpha < 2 \quad \iff \quad -\frac{3}{2} < c < -\frac{1}{2}.$$

We also claim the following intersection **D'** of the upper black blocking boundary $s_1(\alpha) = 1/(1 - 2\alpha) > 0$:

$$(5.13) \quad \mathbf{D}' := s_1 \cap s_{\min\max}, \quad 0 < \alpha < \frac{1}{2} \quad \iff \quad -\infty < c < -\frac{3}{2}.$$

In addition, we mark the following two intersections with the white line $N_1/N = \alpha/(\alpha + 1) = 1/2$ of equal parity $\alpha = N_1/N_3 = 1$:

$$(5.14) \quad \begin{aligned} \mathbf{E} &= s_0 \cap \{\alpha = 1\}, & \lambda &= -(c + 1); \\ \mathbf{F} &= (\alpha = 1, s = 0), & \lambda &= 0. \end{aligned}$$

The elementary proofs all follow the same pattern. We first insert $s_0 = 1/(2 - \alpha) > 0$ from (5.4) and the values of λ in (4.3) or the expression (4.10) for $s_{\min\max}$, as required. For the specified λ -values, we may alternatively invoke (5.5), (5.7). The resulting linear equation for c provides the following explicit expressions:

$$(5.15) \quad \mathbf{A} = s_0 \cap \{\lambda = 0\} : \quad c = (1 - 2\alpha)/\alpha, \quad \alpha = 1/(c + 2);$$

$$(5.16) \quad \mathbf{B} = s_0 \cap \{\lambda = \frac{1}{4}\} : \quad c = -\frac{1}{4}\alpha - 1, \quad \alpha = -4(c + 1);$$

$$(5.17) \quad \mathbf{C} = s_0 \cap \{\lambda = -(c + 1)\} : \quad c = -(\alpha - 5)/(\alpha - 4), \quad \alpha = (4c + 5)/(c + 1);$$

$$(5.18) \quad \mathbf{D} = s_0 \cap s_{\min\max} : \quad c = -(\alpha + 1)/2, \quad \begin{aligned} \alpha &= -2c - 1, \\ \lambda &= (1 + c)/(3 + 2c). \end{aligned}$$

This proves the four claims (5.9)–(5.12) on s_0 . For $s_1 = 1/(1 - 2\alpha)$ from (5.6), we obtain analogously

$$(5.19) \quad \mathbf{D}' = s_1 \cap s_{\min\max} : \quad c = -\frac{1}{2}(\alpha + 1)/\alpha, \quad \begin{aligned} \alpha &= -1/(2c + 1), \\ \lambda &= (1 + c)/(3 + 2c). \end{aligned}$$

This proves the remaining claim (5.13). We have omitted variants $\mathbf{A}', \mathbf{B}', \mathbf{C}' \in s_1$ which will be irrelevant for our subsequent discussion.

It remains to address possible tangencies between level curves $\lambda = \lambda(\alpha, s)$ and the black boundaries of the blocking regions, in the $(N_1/N, \arctan s)$ -plane. At such tangencies, the emanation/termination behavior of the formal rebel dynamics changes, as we will illustrate in the next section. For now, we note that such tangencies \mathbf{T}, \mathbf{T}' are characterized by unique extrema of $\lambda_\iota(\alpha) := \lambda(\alpha, s_\iota(\alpha))$ along the black blocking boundaries $s_\iota(\alpha)$, $\iota = 0, 1$. Elementary calculations of high school type for the rational expressions (5.5), (5.7) of $\lambda_\iota(\alpha)$ provide the explicit expressions

$$(5.20) \quad \mathbf{T} : \quad c = -2(\alpha + 1)/(\alpha + 2) \in (-\frac{3}{2}, -1), \quad \begin{aligned} \alpha &= -2(c + 1)/(c + 2), \\ \lambda &= \frac{1}{4}(c + 2)^2/(2c + 3); \end{aligned}$$

$$(5.21) \quad \mathbf{T}' : \quad c = -2(\alpha + 1)/(2\alpha + 1) \in (-2, -1), \quad \begin{aligned} \alpha &= -\frac{1}{2}(c + 2)/(c + 1), \\ \lambda &= \frac{1}{4}(c + 2)^2/(2c + 3). \end{aligned}$$

See figure 5.4 for an illustration of the tangency point \mathbf{T} .

Since we are interested in minority/majority transitions across the white line $N_1/N = \frac{1}{2}$, below the black blocking curve s_0 , we also determine the values of c where $\mathbf{A}, \dots, \mathbf{D}$, and \mathbf{T} cross $\alpha = 1$:

$\alpha = 1$	\mathbf{A}	\mathbf{B}	\mathbf{C}	\mathbf{D}	\mathbf{T}
c	-1	$-4/3$	$-5/4$	-1	$-4/3$

In conclusion we observe crucial changes in the above intersection behavior at the six critical cubic coefficients $c = -2, -\frac{3}{2}, -\frac{4}{3}, -\frac{5}{4}, -1, -\frac{1}{2}$, as announced in (1.19) and as exemplified in the next section.

6 Results

As announced in (1.19), we illustrate the global heteroclinic dynamics of the 3-cluster system (2.4), in the limit of large dimension $N \rightarrow +\infty$. See the skew product system (3.7), (3.8), and the scaled version (5.2). To represent the seven parameter intervals which are separated by the six critical cubic coefficients $c = -2, -\frac{3}{2}, -\frac{4}{3}, -\frac{5}{4}, -1, -\frac{1}{2}$ of (1.19), we successively illustrate the global dynamics for the seven coefficients

$$(6.1) \quad c = -3, -1.77, -1.37, -1.3, -1.12, -0.75, +1;$$

see figures 6.1–6.8.

We also address those non-blocking regions where, in addition, the driving 2-cluster dynamics $s > 0$ of (3.7) has reached an unstable 2-cluster equilibrium $s = s_* > 0$ according to section 4. We recall from figures 5.3–5.5 how solid magenta arrows along level curves of $\lambda = (\lambda, s)$ indicate heteroclinic rebellions in s -stable regions. Dashed magenta arrows indicate s -unstable regions. This leaves two dashed magenta regions in each of the figures 6.1–6.8.

To enforce s -stability, in regions which are not s -stable originally, according to section 4, we may reverse time in all ODEs. For the coefficients A, B, C in (1.10) this amounts to a reversal of all signs. In (1.8) and the following sections, we just replace $\dot{x}_n = \dots, \dot{s} = \dots, \dot{y} = \dots$ by $-\dot{x}_n = \dots, -\dot{s} = \dots, -\dot{y} = \dots$.

In all seven figures we have shaded the regions in the plane $(N_1/N, \arctan(s))$ where heteroclinic rebel orbits between the two large clusters are blocked, according to section 5.

6.1 The case $-\infty < c < -2$

We begin with the case $-\infty < c = -3 < -2$ of figure 6.1. There are two s -stable non-blocked regions, indicated by solid magenta arrows. The dashed magenta arrows indicate the two s -unstable regions.

The lower s -stable region of solid magenta arrows is located between the lower black blocking boundary s_0 and the right red saddle-node curve. It is split in four by three separating non-solid yellow level curves. In all four subregions, the cluster N_1 wins at the expense of N_3 . The successive heteroclinic dynamics leads to infinite growth of the 2-cluster asynchrony

$$(6.2) \quad s = (\xi_3 - \xi_1)/(\alpha + 1) \longrightarrow +\infty,$$

via a size ratio α which increases asymptotically to $N_1/N_3 = \alpha \nearrow 1/\alpha_c$, given by (4.8).

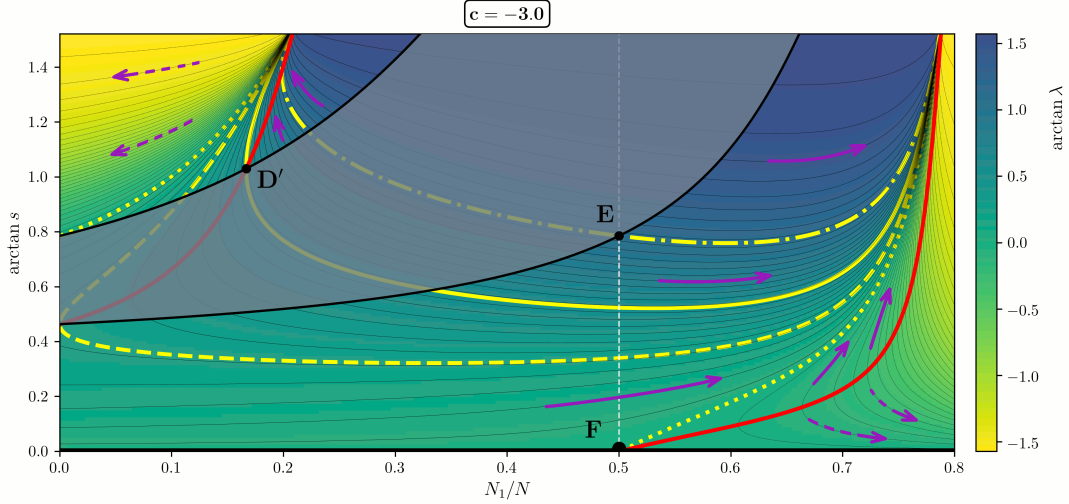


Figure 6.1: Global dynamics in the plane $(N_1/N, \arctan(s))$ for case 6.1, $-\infty < c = -3 < -2$. Color coding and legends as in figures 5.3, 5.5. For definition of the intersection points \mathbf{D}' , \mathbf{E} , \mathbf{F} , see (5.19), (5.14). The shaded region marks blocking of rebel heteroclinic dynamics between the two large clusters of size ratio $\alpha = N_1/N_3$. Magenta arrows indicate the formal flow on the level sets of $\lambda = \lambda(\alpha, s)$. Solid magenta arrows are used in the s -stable region of the asynchronous 2-cluster equilibrium $s = s_* > 0$. Dashed magenta arrows account for the two s -unstable regions. See text for further details.

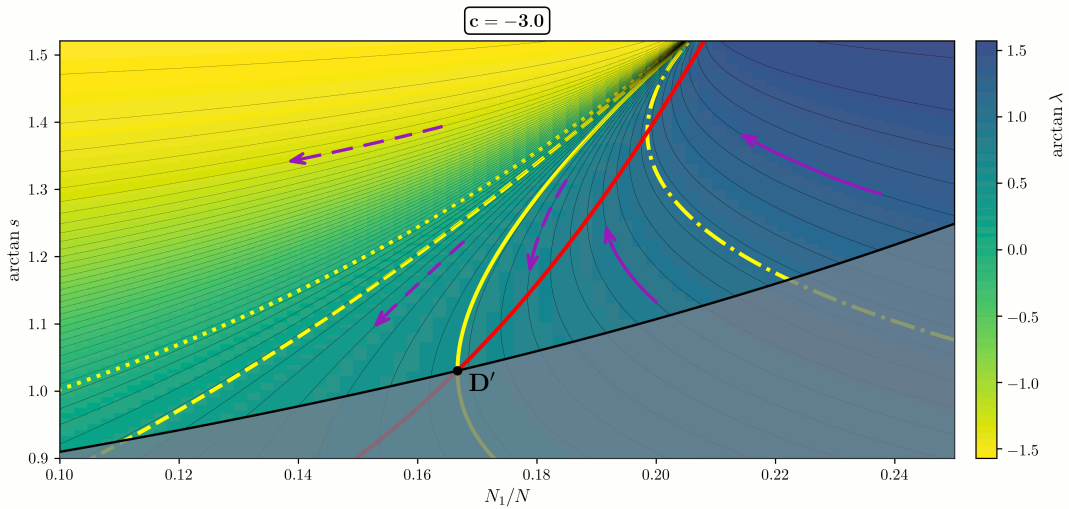


Figure 6.2: Zoom into the upper left s -unstable and s -stable regions of figure 6.1.

Between the dotted and the dashed yellow separatrix, i.e. for $0 < \lambda < 1/4$, all directed level curves of λ emanate from the left boundary $N_1/N = 0$ and terminate at $\alpha = 1/\alpha_c$, $s = +\infty$. This means that the heteroclinic rebel dynamics favors the growth of arbitrarily small clusters (N_1, ξ_1) , “out of the blue”, over the cluster (N_3, ξ_3) , until the cluster asynchrony blows up, $s \nearrow +\infty$, at the maximal sustainable size ratio $\alpha = N_1/N_3 = 1/\alpha_c > 1$: from minority to majority.

Between the dashed and the dotdashed yellow separatrices, i.e. for $1/4 < \lambda < \lambda(\mathbf{E}) = -(c+1)$, minority N_1 can still become majority, until s blows up. This time, however, at least a critical minimal size N_1 of the smaller cluster is required, which depends on the value of λ . Indeed that critical size is determined by the realizable value of $\alpha = N_1/N_3$ at the intersection of the level curve of λ with the black blocking boundary s_0 .

Above the dotdashed separatrix, i.e. for $\lambda > -(c+1) = \lambda(\mathbf{E})$, the rebel growth of N_1 does not cross the white line $N_1/N = \frac{1}{2}$. The cluster size N_1 , initiating to the right of \mathbf{E} on the blocking boundary s_0 , must exceed N_3 from the start. To the right of the dotted separatrix from \mathbf{F} , i.e. for given $\lambda < 0$, the minimally required cluster size of N_1 is determined by the value α of the cluster ratio N_1/N_3 on the right red saddle node curve $s_{\min\max}$ corresponding to $\lambda_{\min\max} = \lambda$.

The upper s -stable region of solid magenta arrows is located in the triangular wedge above \mathbf{D}' , between the left red saddle-node curve $s_{\min\max}$ and the upper black blocking boundary s_1 . Rebellions there originate from s_1 and decrease $\alpha = N_1/N_3 < 1$, until they terminate at $s_{\min\max} > 0$, where 2-cluster solutions disappear into saddle-node bifurcations. See the zoom 6.2 of figure 6.1.

Similar remarks apply to the remaining two non-blocking regions which are s -unstable. The dashed magenta arrows indicate the resulting formal rebel dynamics. The upper left s -unstable region is bounded below by the black blocking boundary $s = s_1(\alpha)$ and the upper red saddle-node curve $s = s_{\min\max}(\alpha)$; see (5.6) and (4.10). In (5.13) and (5.19) we have denoted their intersection by \mathbf{D}' . The two yellow separatrix levels $\lambda(\alpha, s) = 0$, dotted, and $\lambda(\alpha, s) = \lambda(\mathbf{D}')$, solid, define three subregions, which are distinguished by the eventual fate of the heteroclinic rebel dynamics. The rebellion may terminate at the left boundary $\alpha = 0$, at the black blocking boundary $s_1(\alpha)$ to the left of \mathbf{D}' , or at the left red saddle-node cluster configuration $s_{\min\max}(\alpha)$ to the right of \mathbf{D}' . In all three cases, the ongoing decay of $\alpha = N_1/N_3$ originates from asynchrony $s = +\infty$, at finite size ratio $\alpha = \alpha_c < 1$.

The lower right region of dashed magenta rebel dynamics does not involve unbounded asynchrony, for fixed λ . All rebellions favor N_1 over N_3 , this time, and terminate at $\alpha = N_1/N_3 = \infty$ alias $N_3 = 0$, $N_1 = N$. Heteroclinic rebels defect from N_3 to the larger cluster N_1 . Defection originates from the red saddle-node boundary $s_{\min\max}(\alpha) > 0$, to the right of \mathbf{F} , for some λ -dependent minimal $\alpha = N_1/N_3 > 1$. Note that majority $N_1 > N_3$ prevails, because the white line $N_1/N = \frac{1}{2}$ is not crossed.

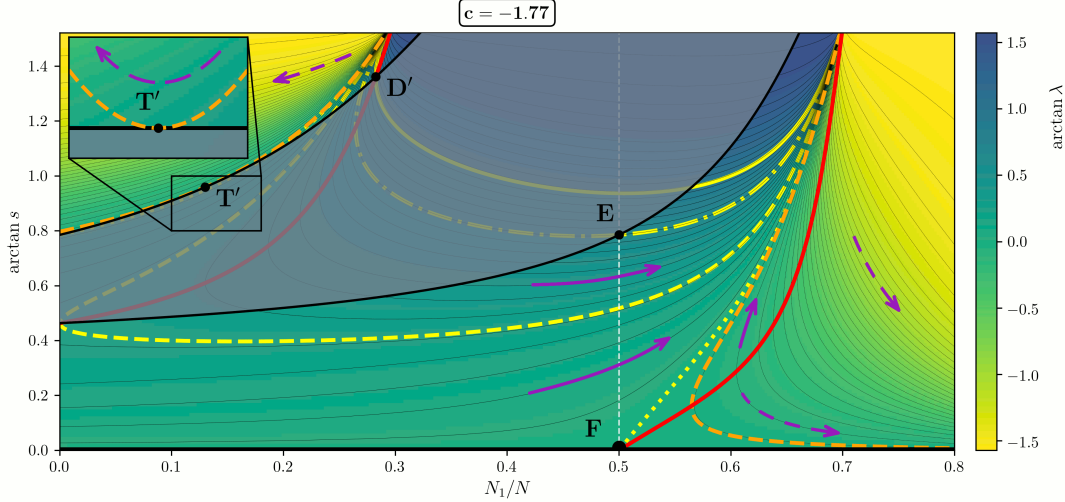


Figure 6.3: Global dynamics in the plane $(N_1/N, \arctan(s))$ for case 6.2, $-2 < c = -1.77 < -3/2$. For definition of the tangency \mathbf{T}' between the upper solid black blocking boundary and the level set $\lambda(\alpha, s) = \lambda(\mathbf{T}')$; see (5.21).

6.2 The case $-2 < c < -3/2$

We address the case $-2 < c = -1.77 < -3/2$ of figure 6.3 next. The description is identical to the previous case $c = -3$, in the original s -stable regions with solid magenta arrow, and in the lower right s -unstable region with dashed arrows. Note however the intersection point \mathbf{D}' and the tangency point \mathbf{T}' on the upper black blocking boundary s_1 . These points only affect level sets in the upper left s -unstable region of dashed magenta rebel arrows. The corner point \mathbf{D}' and its level set $\lambda(\alpha, s) = \lambda(\mathbf{D}')$ retain their previous significance. See in particular the previous zoom in figure 6.2. However, the new tangency point \mathbf{T}' comes with a level set $\lambda(\alpha, s) = \lambda(\mathbf{T}')$ which consists of two branches. Only above $\lambda = \lambda(\mathbf{T}')$ do we still observe termination at $N_1 = 0$, originating from asynchrony $s = +\infty$ at $\alpha = \alpha_c$. Below the left branch of $\lambda = \lambda(\mathbf{T}')$, such rebellion originates from the blocking boundary, instead. Below the right branch, the rebellion still originates from $s = +\infty$, $\alpha = \alpha_c$ as before, but terminates at a minimal cluster ratio $\alpha = \alpha(\lambda) > 0$.

6.3 The case $-3/2 < c < -4/3$

The case $-3/2 < c = -1.37 < -4/3$ of figure 6.4 features only a single s -stable region of solid magenta arrows, and two s -unstable time-reversed regions of dashed magenta arrows. The only s -stable region, lower triangular between the lower black blocking boundary s_0 and the right red saddle-node curve, has now detached from the singular tip $s = +\infty$ at $\alpha = 1/\alpha_c$. The new tip is at \mathbf{D} ; see (5.12) and (5.18). Along s_0 , the intersection points $\mathbf{A}, \mathbf{B}, \mathbf{C}$ have appeared, with the yellow λ -levels $\lambda = 0 = \lambda(\mathbf{F})$ (dotted), $\lambda = 1/4$ (dashed) and $\lambda = -(c + 1) = \lambda(\mathbf{E})$ (dotdashed), respectively. See (5.9)–(5.10) and (5.15)–(5.17). The three yellow separatrices define four subregions.

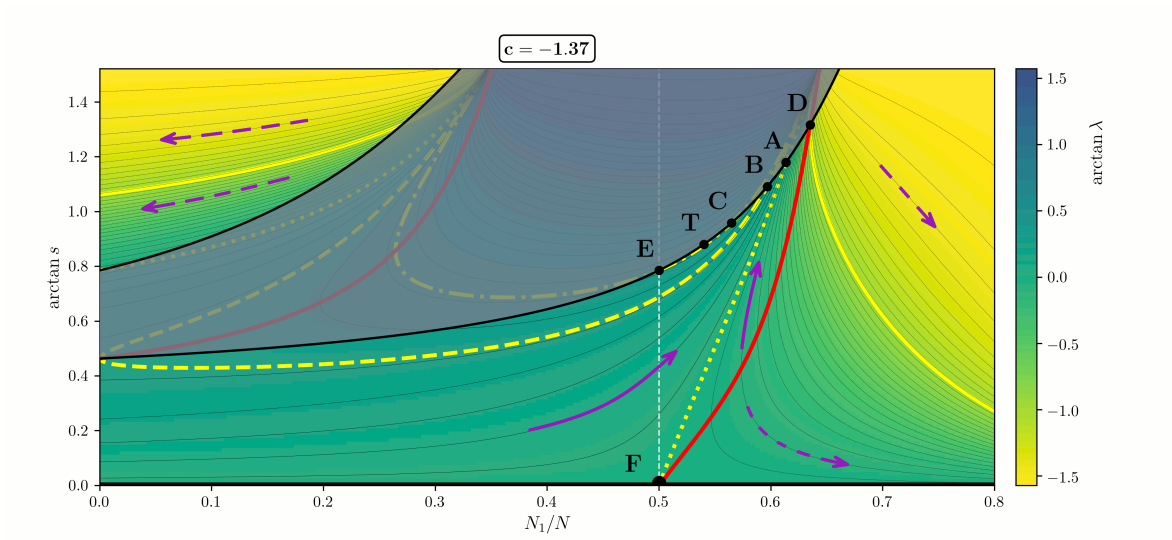


Figure 6.4: Global dynamics in the plane $(N_1/N, \arctan(s))$ for case 6.3, $-3/2 < c = -1.37 < -4/3$.

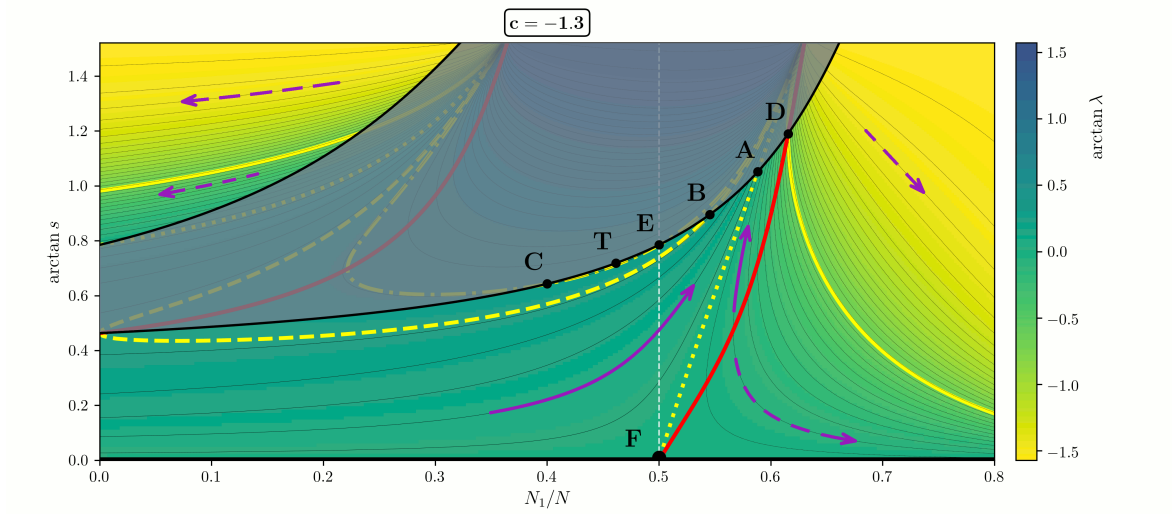


Figure 6.5: Global dynamics in the plane $(N_1/N, \arctan(s))$ for case 6.4, $-4/3 < c = -1.3 < -5/4$. See also figure 5.3.

For $\lambda < 0$, i.e. in the triangular subregion **ADF**, rebellions start from the red saddle-node curve **DF** and terminate at the black blocking boundary segment **AD**. In the pentagonal subregion $0 < \lambda < \frac{1}{4}$, all rebellions start from “blue sky”, at $\alpha = N_1/N_3 = 0$, with tiny N_1 . They gain majority as they cross the dashed white break-even line $N_1 = N_3$, and terminate at the black blocking boundary segment **AB**. For $\frac{1}{4} < \lambda < -(c+1) = \lambda(\mathbf{E})$, rebellions still gain majority across the white line, but they start on the black blocking boundary s_0 to the left of **E** and terminate on the segment **BC** of s_0 . The black blocking segment **CE** to the right of **E**, finally, exhibits a new tangency **T** with the level curves of λ . For $-(c+1) = \lambda(\mathbf{E}) < \lambda < \lambda(\mathbf{T})$ this leads to rebellions, from N_3 to increasing $N_1 > N_3$ already in majority, which start and terminate at the black blocking boundary: from **ET** to **CT**. Except for the location to the right of the white break-even line, the dynamics follows the zoom in figure 5.4.

The upper region of dashed magenta arrows has simplified: all rebellions now originate from the black blocking boundary s_1 , with finite α and s , and terminate at $\alpha = 0$. The lower dashed magenta arrow region, likewise, terminates at $\alpha = +\infty$, $N_3 = 0$. For $\lambda < \lambda(\mathbf{D})$, the rebellions originate from black blocking s_0 and, for $\lambda(\mathbf{D}) < \lambda < 0$, at saddle-node (red).

6.4 The case $-4/3 < c < -5/4$

The case $-4/3 < c = -1.3 < -5/4$, of figure 6.5 has been prepared in section 5; see figure 5.3. The two regions of dashed magenta arrows correspond to the previous case, verbatim.

The s -stable triangular region of solid magenta arrows looks quite similar to figure 6.4, except for the position of the dashed white line **EF** of equal parity $N_1 = N_3$. The segment **CT** on the black blocking boundary has in fact moved from the right of **E** to the left of **E**, i.e. from size ratios $\alpha > 1$ to $\alpha < 1$. Of the four s -stable regions separated by the three yellow level curves $\lambda = 0, \frac{1}{4}, -(c+1)$, this only effects the region $-c+1 < \lambda < \lambda(\mathbf{T})$ which now features a minority N_1 , still growing, rather than a majority. Rebellions lead from **CT** to **ET**, this time.

6.5 The case $-5/4 < c < -1$

For $-5/4 < c = -1.12 < -1$, as in figure 6.6, the situation in the two regions of dashed magenta arrows remains the same, qualitatively, as in the two previous figures 6.4 and 6.5. In the remaining unique s -stable region of solid magenta arrows, the dotdashed yellow level $\lambda = -(c+1) = \lambda(\mathbf{E})$ has dropped below the dashed yellow level $\lambda = \frac{1}{4}$, as c increased through $-5/4$. The region of rebellion from “blue sky” minority $N_1 = 0$ to majority $N_1 > N_3$, across the dashed white line **EF**, therefore requires $0 < \lambda < -(c+1)$, now. Termination occurs at the black blocking segment **EA** of s_0 . The second intersection point **C** of s_0 with the yellow level $\lambda = -(c+1) = \lambda(\mathbf{E})$ has disappeared. The region $\frac{1}{4} < \lambda < \lambda(\mathbf{T})$ now features growth of the minority N_1 from the black blocking segment of s_0 on the left of **T** to **TB**.

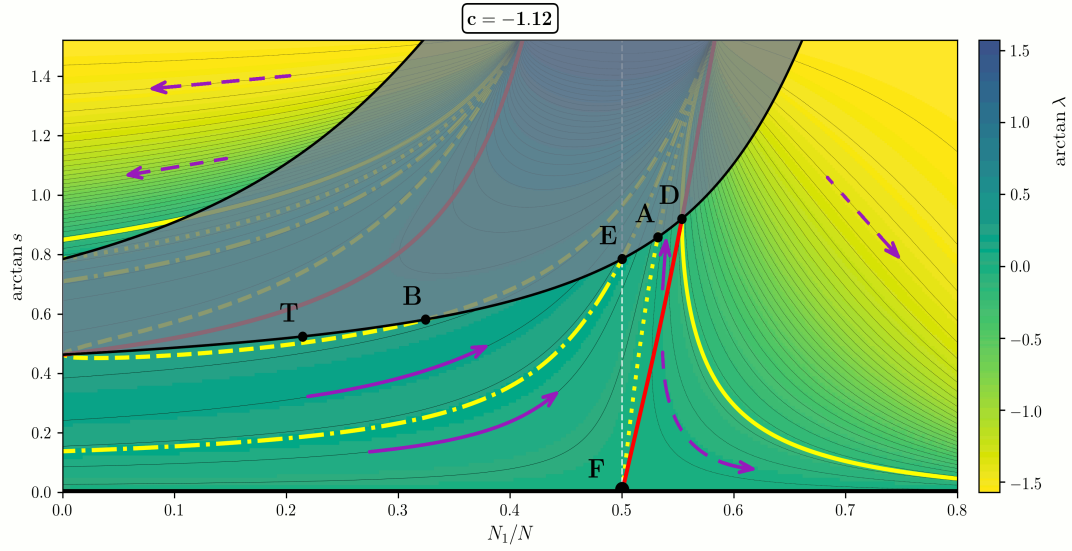


Figure 6.6: Global dynamics in the plane $(N_1/N, \arctan(s))$ for case 6.5, $-5/4 < c = -1.12 < -1$.

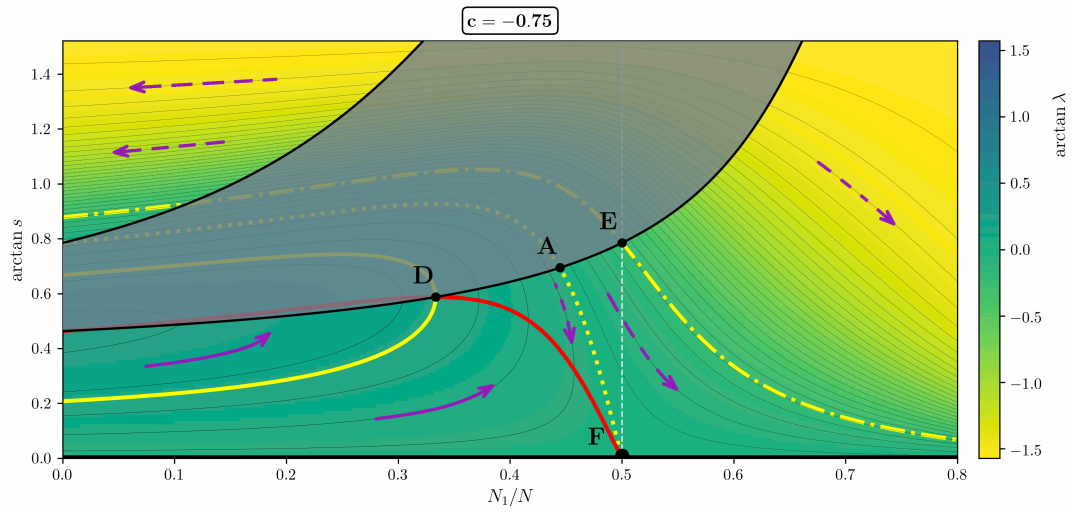


Figure 6.7: Global dynamics in the plane $(N_1/N\alpha, \arctan(s))$ for case 6.6, $-1 < c = -0.75 < -1/2$.

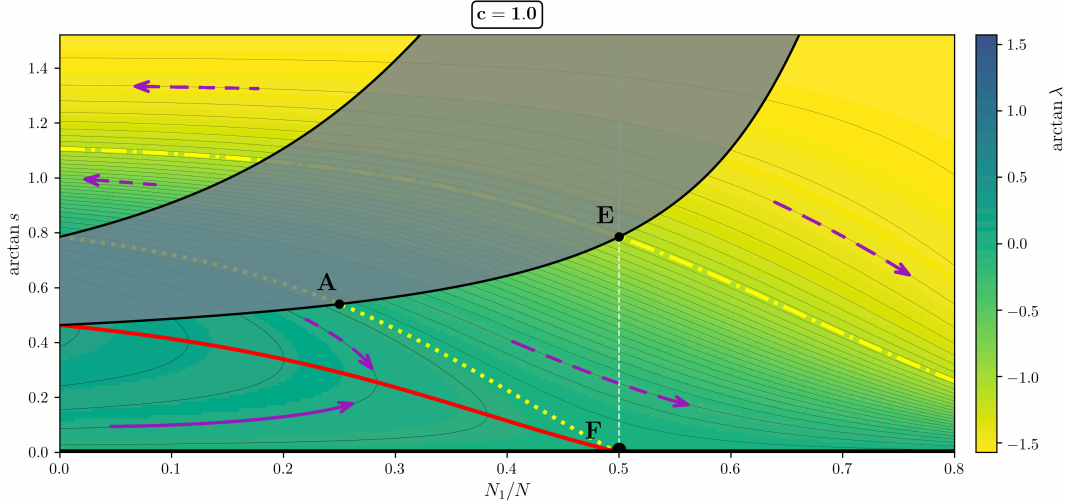


Figure 6.8: Global dynamics in the plane $(N_1/N, \arctan(s))$ for case 6.7, $-1/2 < c = +1 < +\infty$.

6.6 The case $-1 < c < -1/2$

The case $-1 < c = -0.75 < -1/2$ of figure 6.7 has also been prepared in section 5; see figure 5.5. The upper left region of time-reversed dashed magenta arrows remains the same, qualitatively, as in figures 6.4–6.6. The original s -stable region of solid magenta arrows is now contained in the region N_1/N to the left of the dashed white line $N_1 = N_3$ of equal parity. Thus N_1 is, and remains, in minority $N_1 < N_3$. The only yellow separatrix $\lambda = \lambda(\mathbf{D}) > 0$ (solid) highlights the intersection \mathbf{D} of the lower black blocking boundary s_0 with the only remaining red saddle-node curve $s_{\min\max}$; see (5.12) and (5.18). All rebellions start from “blue sky” i.e. at vanishing N_1 . In the subregion $0 < \lambda < \lambda(\mathbf{D})$ they terminate at the red saddle-nodes. In the complementary subregion $\lambda(\mathbf{D}) < \lambda < \frac{1}{4}$, they terminate at the black blocking boundary.

The second time-reversed region of dashed magenta arrows, on the right, is now subdivided into three subregions by the two yellow separatrices \mathbf{AF} of $\lambda = 0$ (dotted) and $\lambda = -(c + 1) = \lambda(\mathbf{E})$ (dotdashed). For $\lambda(\mathbf{D}) > \lambda > \lambda(\mathbf{A}) = 0$, the longer cluster N_3 decays by heteroclinic rebellions which proceed from the segment \mathbf{AD} of the black blocking boundary s_0 to the red saddle-nodes, where N_3 is still in majority. For $\lambda < \lambda(\mathbf{A}) = 0$, rebellions terminate at $N_3 = 0$. In the subregion $\lambda(\mathbf{A}) = 0 > c > -(c + 1) = \lambda(\mathbf{E})$ the majority cluster N_3 from the black blocking segment \mathbf{AE} of s_0 crosses the dashed white line of equal parity until it terminates as minority. For $\lambda(\mathbf{E}) = -(c + 1) > \lambda$, the cluster N_3 remains a minority, originating from the black blocking segment of s_0 , to the right of \mathbf{E} , at a finite value of s .

6.7 The case $-1/2 < c < +\infty$

The final case is $-1/2 < c = 1 < +\infty$, as in figure 6.8. As for all $c > -3/2$ we obtain a single s -stable region, with solid magenta arrows, and two time-reversed s -unstable regions with dashed magenta arrows; see figures 6.4–6.7. The upper left

dashed magenta region remains unchanged. The solid magenta region has lost \mathbf{D} from its boundary: all rebellions originate from red saddle-nodes and terminate at $N_1 = 0, \alpha = 0$, with N_1 remaining in minority.

The wedge of the second dashed magenta region, on the right, now reaches left all the way to the tip at $\alpha = 0, s = \frac{1}{2}$ where $\lambda = \frac{1}{4}$. The two yellow level curves $\lambda = 0 = \lambda(\mathbf{A})$ and $\lambda = -(c + 1) = \lambda(\mathbf{E}) < -\frac{1}{2}$ divide the region into three subregions, just as in the previous case $-1 < c < -1/2$ of figure 6.7. The only difference, now, is that rebellions for $0 < \lambda < \frac{1}{4}$ originate from anywhere on the black blocking boundary, to the left of \mathbf{A} , i.e. at any size ratio $0 < \alpha = N_1/N_3 < \alpha(\mathbf{A}) = 1/(c + 2) < 2/3$; not just at $0 < -2c - 1 = \alpha(\mathbf{D}) < \alpha < \alpha(\mathbf{A}) = 1/(c + 2) < 1$ bounded away from $\alpha = 0$, as they did in the previous case. The two other subregions of $\lambda < 0$, as before, show how the cluster N_3 can decay to $N_3 = 0$ from the maximal value of $N_3/N = 1 - \alpha/(\alpha + 1)$ on the black blocking boundary, which is sustainable at the given level of $\lambda < 0$. If we reverse time, to make this s -unstable region s -stable, then the growth of $N_3 = 0$ to the maximally sustainable N_3 reveals the limitations of rebel dynamics defecting to minority.

7 Example: Stuart-Landau oscillators with global coupling

In this section, we study N globally coupled, identical Stuart-Landau oscillators

$$(7.1) \quad \dot{W}_n = (1 - (1 + i\gamma)|W_n|^2)W_n + \beta \cdot (\langle W \rangle - W_n).$$

Here $W_n \in \mathbb{C}$ indicate phase and amplitude of the n -th oscillator, $n = 1, \dots, N$. We consider real amplitude dependence γ of individual periods, complex coupling $\beta \in \mathbb{C}$, and we abbreviate the average $\langle W \rangle := \frac{1}{N} \sum W_n$, as before. Note S_N -equivariance of (7.1) under the action analogous to (1.1).

For a background and motivation we recall how (7.1) often serves, in physics, as a “normal form” for oscillatory systems close to the onset of oscillation and under the influence of a linear coupling through the mean field [GMK08]. This normal form has been established to be a good approximation in a multitude of contexts from various disciplines, whether it be in physics, chemistry, biology, neuroscience, social dynamics, or engineering. For an overview see, e.g. [PRK03, PR15] or references 1-15 in [KGO15]. Our motivation to study (7.1) is to gain a deeper understanding of the dynamics of oscillatory electrochemical systems. Indeed global, linear coupling often controls the evolution of the electrostatic potential of the working electrode, a crucial dynamic variable in electrochemical systems [WKH00, Kri01, PLK04, VBBK05, MGMK09, KK&al14, SZHK14, SK15, PH&al17, LSMK18, NKV19, HGK19]. The global coupling originates from the electric control of the device: any potential drop in the electrolyte or the external electric circuit is fed back to the evolution of the electrode potential at any location. Yet, there are many other situations where the dynamics of the electric potential is governed in almost the same manner as in electrochemical systems. Examples include semiconductor devices [Sch01], gas discharge tubes

[PBA10], or arrays of Josephson junctions [BVB97]. Along with these numerous applications go various theoretical studies of the globally coupled Stuart-Landau ensemble [NK93, NK94, NK95, HR92, SF89, MS90, MMS91, DN04, DN06, KGO15, KHK19].

Specifically, we consider bifurcations from the globally synchronous periodic solution

$$(7.2) \quad W_n(t) = \exp -(\mathrm{i}\gamma t)$$

of amplitude 1 and minimal period $2\pi/\gamma$. Somewhat unconventionally, we rewrite (7.1) in ‘‘polar coordinates’’ $Z_n = R_n + \mathrm{i}\Psi_n$ via $W_n = \exp(Z_n)$ as

$$(7.3) \quad \dot{Z}_n = \dot{W}_n/W_n = 1 - (1 + \mathrm{i}\gamma)|W_n|^2 + \beta(-1 + \frac{1}{N} \sum_{k=1}^N W_k/W_n).$$

We now invoke the notation (1.9) and define

$$(7.4) \quad \begin{aligned} R &:= \frac{1}{N} \sum R_n, & r_n &:= \widetilde{R}_n = R_n - R, \\ \Phi &:= \frac{1}{N} \sum \Phi_n, & \varphi_n &:= \widetilde{\Phi}_n = \Phi_n - \Phi, \\ Z &:= R + \mathrm{i}\Phi, & z_n &:= r_n + \mathrm{i}\varphi_n, \quad \mathbf{z} = (z_n)_{n=1}^N, \end{aligned}$$

to derive

$$(7.5) \quad \dot{\varphi}_n = -\gamma e^{2R} \widetilde{e^{2r_n}} + \mathrm{Im}(\beta \langle e^z \rangle \widetilde{e^{-z_n}}),$$

$$(7.6) \quad \dot{r}_n = -e^{2R} \widetilde{e^{2r_n}} + \mathrm{Re}(\beta \langle e^z \rangle \widetilde{e^{-z_n}}),$$

$$(7.7) \quad \dot{R} = 1 - e^{2R} \langle e^{2r} \rangle + \mathrm{Re}(\beta(\langle e^z \rangle \langle e^{-z} \rangle - 1)),$$

and the average phase

$$(7.8) \quad \dot{\Phi} = -\gamma e^{2R} \langle e^{2r} \rangle + \mathrm{Im}(\beta(\langle e^z \rangle \langle e^{-z} \rangle - 1)).$$

Here we have slightly extended the notation (1.9) to include

$$(7.9) \quad \begin{aligned} \langle e^z \rangle &:= \frac{1}{N} \sum_{n=1}^N e^{z_n} = \frac{1}{N} \sum_{n=1}^N \sum_{m=0}^{\infty} \frac{1}{m!} z_n^m = \sum_{m=0}^{\infty} \frac{1}{m!} \langle z^m \rangle, \\ \widetilde{e^{z_n}} &:= e^{z_n} - \langle e^z \rangle = \sum_{m=0}^{\infty} \frac{1}{m!} (z_n^m - \langle z^m \rangle) = \sum_{m=0}^{\infty} \frac{1}{m!} \widetilde{z_n^m}. \end{aligned}$$

The globally synchronous solution (7.2) becomes the *trivial equilibrium* $\mathbf{z} = 0, R = 0$ of (7.5)–(7.7), in this notation. The average phase $\Phi(t)$ does not appear in these ODEs, due to S^1 -equivariance of the original Stuart-Landau system (7.1) under uniform phase shifts. We will therefore ignore the average phase $\Phi(t)$, henceforth. We only keep in mind how equilibria of \mathbf{z}, R , and heteroclinic orbits between them, actually indicate periodic orbits and their heteroclinic connections, via the skew product structure of $\dot{\Phi} = \dots$, driven by the Φ independent dynamics of \mathbf{z}, R , only.

Our task, in the present section, is the derivation of the reduced flow (1.10), i.e.

$$(7.10) \quad \dot{x}_n = \mu_+ x_n + A \widetilde{x_n^2} + B \widetilde{x_n^3} + C \langle x^2 \rangle x_n + \dots$$

in a center manifold of the trivial equilibrium $\mathbf{z} = 0$, $R = 0$ of the system (7.5)–(7.7), at a zero eigenvalue μ_+ of the linearization. See for example [Carr, ChHa82, Van89] for a background on center manifolds.

An outline of this standard procedure is as follows. We replace $z_n = r_n + i\varphi_n \in \mathbb{C}$ by suitable linear real coordinates (x_n, y_n) such that the eigenspace of the mandatory eigenvalue $\mu_+ = 0$ is given by $\mathbf{y} = 0$, $R = 0$. The remaining eigenvalues will be $\mu_- < 0$, for $\mathbf{x} = 0$, $R = 0$, and $\mu_0 = -2$, for $\mathbf{x} = \mathbf{y} = 0$. Since $\langle z \rangle = 0$, by construction of $z_n = \widetilde{R}_n + i\widetilde{\Phi}_n$, we will inherit $\langle x \rangle = 0 = \langle y \rangle$, i.e. $\mathbf{x}, \mathbf{y} \in X_0$ will realize the standard representation of S_N ; see (1.1), (1.7). Since the S_N -invariant center manifold can be written as a graph of (\mathbf{y}, R) over \mathbf{x} , tangent to the eigenspace of $\mu_+ = 0$ at the trivial equilibrium, truncation to second order yields

$$(7.11) \quad y_n = a\widetilde{x}_n^2 + \dots ,$$

$$(7.12) \quad R = b\langle x^2 \rangle + \dots ,$$

with suitable real coefficients a, b calculated below. Substitution of (7.11), (7.12) into the ODE $\dot{x}_n = \dots$ with vanishing linear part then allows us to determine the coefficients A, B, C of the reduced flow (7.10) in the center manifold, up to third order in \mathbf{x} , as required for our analysis of (1.10), (1.8). We can then invoke the results of sections 1–6 to detect rebel heteroclinic dynamics between periodic 2-cluster solutions of the globally coupled Stuart-Landau system (7.1). See [SEC03] for another example in a Darwinian setting.

To substantiate the above outline we start from the following linear change of coordinates:

$$(7.13) \quad \begin{aligned} 2dx_n &:= -r_n + \frac{d+1}{\gamma'}\varphi_n, & r_n &= (1-d)x_n + (1+d)y_n, \\ 2dy_n &:= +r_n + \frac{d-1}{\gamma'}\varphi_n, & \varphi_n &= \gamma'x_n + \gamma'y_n. \end{aligned}$$

for $n = 1, \dots, N$. The system on the right defines the inverse of the system on the left. Here d abbreviates the discriminant root

$$(7.14) \quad d := \sqrt{1 - \beta_I^2 - 2\gamma\beta_I} > 0,$$

writing the real and imaginary parts of the complex linear coupling as $\beta = \beta_R + i\beta_I$. Of course we assume *positive discriminant*, i.e.

$$(7.15) \quad \beta_I^2 + 2\gamma\beta_I < 1.$$

The coefficient γ' in (7.13) is defined as

$$(7.16) \quad \gamma' := \beta_I + 2\gamma.$$

The two real eigenvalues of the linearization of (7.5), (7.6) at the trivial equilibrium $\mathbf{z} = 0, R = 0$ are

$$(7.17) \quad \mu_{\pm} = -(\beta_R + 1) \pm d.$$

Note that each of the real eigenvalues $\mu_- < \mu_+$ is of algebraic and geometric multiplicity $N - 1$. Indeed the eigenspaces $\mathbf{x} = 0$, $R = 0$ and $\mathbf{y} = 0$, $R = 0$ are each isomorphic to the standard irreducible representation X_0 of S_N . The requisite eigenvalue $\mu_+ = 0$, at bifurcation, is picked such that $\mu_- < 0 = \mu_+$ and the algebraically simple eigenvalue $\mu_0 = -2$, in the synchrony direction of R , ensure exponential stability of the reduced flow on the center manifold of μ_+ . We collect some relations among the available coefficients:

$$(7.18) \quad \begin{aligned} \beta_R &= d - 1, \\ \gamma' \beta_I &= (\beta_I + 2\gamma)\beta_I = 1 - d^2 = -(\beta_R + 2)\beta_R, \\ \beta &= (d - 1)(1 - i(d + 1)/\gamma'). \end{aligned}$$

Indeed, the first line follows from $\mu_+ = 0$ and (7.17). The second line uses definition (7.16) of γ' , the definition (7.14) of d , and the first line. The third line follows from the first and the second. In summary, (7.16) and (7.18) allow us to express the three free real parameters γ, β_R, β_I of (7.1) by the two real parameters γ' and d , at $\mu_+ = 0$, with the only remaining constraint $d > 0 \neq \gamma'$. We will therefore express the remaining coefficients a, b of (7.11), (7.12), and A, B, C of (7.10) in terms of γ' and d .

To calculate a, b we use existence and C^k differentiability of the center manifold, for any $k > 0$. See [Van89]. We first expand the transformed ODE

$$(7.19) \quad \begin{aligned} 0 + \dots &= 2dy'_n(\mathbf{x})\dot{\mathbf{x}} = 2dy'_n = \dot{r}_n + \frac{d-1}{\gamma'}\dot{\varphi}_n = \\ &= -(1 + (\lambda - 1)\frac{\gamma}{\gamma'})e^{2R}\widetilde{e^{2r_n}} + \operatorname{Re}\left(\left(1 - i\frac{d-1}{\gamma'}\right)\beta(\langle e^z \rangle \widetilde{e^{-z_n}})\right) = \\ &= \mu_- y_n + \dots \end{aligned}$$

Here we have substituted (7.6), (7.5) on the right, after the transformation (7.13). On the left, we have inserted the quadratic expansion (7.11). Note that $\dot{\mathbf{x}} = \mu_+ \mathbf{x} + \dots$ with $\mu_+ = 0$ is at least quadratic. Moreover, tangency of the center manifold to the eigenspace $y_n = R = 0$ implies $y'_n(0) = 0$. Therefore, the left hand side of (7.19) starts at (omitted) cubic order. Substitution of (7.13), (7.18), and the expansion (7.11) on the right side of (7.19), yield the result

$$(7.20) \quad a = \frac{1-d}{8\gamma'^2 d^2} (\gamma'^2 + (d-1)^2) (\gamma'^2 + 3(d^2 - 1)) ,$$

by comparison of quadratic coefficients. For R , we analogously obtain

$$(7.21) \quad 0 + \dots = R'(\mathbf{x})\dot{\mathbf{x}} = \dot{R} = 1 - e^{2R}\langle e^{2r} \rangle + \operatorname{Re}(\beta(\langle e^z \rangle \langle e^{-z} \rangle - 1)) ,$$

with a left hand side of at least cubic order. Substitutions and comparison of second order coefficients yield

$$(7.22) \quad b = \frac{1}{2}(1 - d) (\gamma'^2 + (d-1)(d+5)) .$$

To calculate the reduced flow $\dot{x}_n = f_n(\mathbf{x})$ in the center manifold, to order $k \geq 2$, it is always sufficient to expand the center manifold itself to order $k - 1$. To determine the

quadratic coefficient A and the cubic coefficients B, C in (1.10), we expand

$$\begin{aligned}
(7.23) \quad 2d\dot{x}_n &= -\dot{r}_n + \frac{d+1}{\gamma'} \dot{\varphi}_n = \\
&= -\left(-1 + (d+1)\frac{\gamma}{\gamma'}\right) e^{2R} \widetilde{e^{2r_k}} + \operatorname{Re}\left(-1 - i\frac{d+1}{\gamma'} \beta(\langle e^z \rangle \widetilde{e^{-z_k}})\right) = \\
&= \mu_+ x_n + A \widetilde{x_n^2} + B \widetilde{x_n^3} + C \langle x^2 \rangle x_n + \dots
\end{aligned}$$

to cubic order. We use the substitutions (7.13) and (7.18) and insert the quadratic expansions (7.11), (7.12) to finally obtain, with the prerequisite stamina,

$$(7.24) \quad A = \frac{d-1}{4\gamma'^2 d} (\gamma'^2 + (d+1)^2) (\gamma'^2 - 3(d-1)^2) ;$$

$$\begin{aligned}
(7.25) \quad B &= -\frac{1}{d} \left(\frac{d-1}{4\gamma'^2 d}\right)^2 (\gamma'^2 + (d+1)^2) (\gamma'^2 + (d-1)^2) \cdot \\
&\quad \cdot ((\gamma' + d)^2 + 2d^2 - 3) ((\gamma' - d)^2 + 2d^2 - 3) ;
\end{aligned}$$

$$\begin{aligned}
(7.26) \quad C &= \frac{1}{d} \left(\frac{d-1}{4\gamma'^2 d}\right)^2 \left(\gamma'^8 - 4(2d^3 - 7d^2 + 1)\gamma'^6 - 2(8d^5 + d^4 - 56d^3 + 22d^2 + 1)\gamma'^4 - \right. \\
&\quad \left. - 4(d+1)^3(d-1)^2(2d^2 + 3d - 3)\gamma'^2 + 9(d^2 - 1)^4 \right).
\end{aligned}$$

In particular, scaling (1.11) for nonzero A, B and truncation to cubic order lead to the cubic normal form (1.8) studied in the previous sections. The remaining cubic coefficient $c = C/B$, according to (1.12), is then given by the long but explicit expression

$$(7.27) \quad c = \frac{\gamma'^8 - 4(2d^3 - 7d^2 + 1)\gamma'^6 - 2(8d^5 + d^4 - 56d^3 + 22d^2 + 1)\gamma'^4 - 4(d+1)^3(d-1)^2(2d^2 + 3d - 3)\gamma'^2 + 9(d^2 - 1)^4}{-(\gamma'^2 + (d+1)^2)(\gamma'^2 + (d-1)^2)((\gamma' + d)^2 + 2d^2 - 3)((\gamma' - d)^2 + 2d^2 - 3)} .$$

Our results are summarized in the contour plot of figure 7.1. First we note that the rational function $c = c(\gamma', d)$ of (7.27) is even in γ' . We can therefore omit negative γ' and only consider $d, \gamma' > 0$. We recall the expressions (7.14) and (7.18) for d and γ' , in terms of the original coefficients $\gamma \in \mathbb{R}$ and $\beta \in \mathbb{C}$ of the coupled Stuart-Landau system (7.1). The coefficient γ regulates the soft-/hard-spring characteristic of the individual Stuart-Landau oscillator, i.e. the monotone dependence of period on amplitude. Complex linear all-to-all coupling is regulated by β . Colors in figure 7.1 indicate the seven intervals of $c \in \mathbb{R}$ which are complementary to the six critical levels

$$(7.28) \quad c = -2, -\frac{3}{2}, -\frac{4}{3}, -\frac{5}{4}, -1, -\frac{1}{2},$$

as identified in section 5. We have subdivided the intervals $c < -2$ and $c > -1/2$, for clarity.

For further illustration we briefly relate our present results to the discussion of the *2-cluster singularity* in [KHK19]. By definition, the 2-cluster singularity refers to the bifurcation point $\lambda = 0$ of an odd nonlinearity $A = 0$ in the dynamics (1.10) on the center manifold. The very value $A = 0$, however, is conspicuously absent in our scaled asymmetric version (1.8), due to the singular scaling (1.11) with $\tau = B/A^2$. From the outset, we note that any analysis of 2-cluster equilibria is subsumed as $N_2 = 0$ in our present setting. Therefore such results hold for all N , and are not restricted

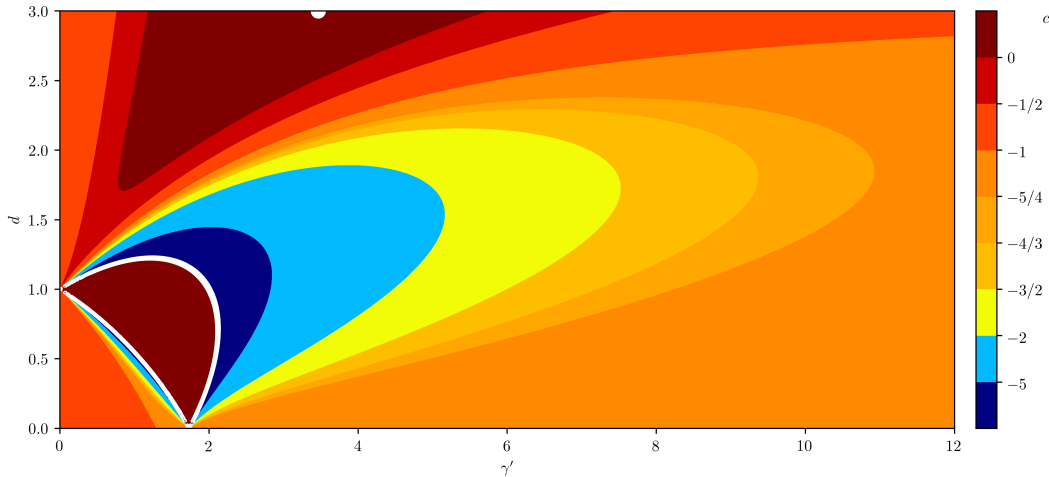


Figure 7.1: Level sets of the cubic coefficient $c = c(\gamma', d)$ in the cubic S_N normal form (1.8), as a function of the positive parameters γ' and d . See (7.27). Since $c(\gamma', d) = c(-\gamma', d)$ is quadratic in γ' , we only plot positive γ', d . See (7.14) and (7.18) for expressions of d and γ' in terms of the original coefficients $\gamma \in \mathbb{R}$, of period-amplitude dependence, and $\beta \in \mathbb{C}$, of complex linear coupling, in the Stuart-Landau setting (7.1). The singular set $c = \pm\infty$, alias $B = 0$, is indicated by the white crescent. For resulting dynamics in the colored intervals of c see the representative figures 6.1–6.8 of section 6. The white dot at $d = 3$, $\gamma' = 2\sqrt{3}$ indicates the 2-cluster singularity $c = 1$ of fig. 6.8.

to any asymptotics of large N . This extends to the bifurcation curves of rebel 3-cluster stationary solutions, at the blocking curves. Indeed, the defining kernels of the linearization are independent of the size of the bifurcating cluster; see (4.39) and (4.40) in [Elm01].

We can easily determine the 2-cluster singularities in the parameters γ', d of figure 7.1. Indeed, $A = 0$ in our derivation (7.24) is equivalent to the pair of straight lines

$$(7.29) \quad \gamma'^2 = 3(d - 1)^2.$$

Quite remarkably, insertion of (7.29), to eliminate γ' , collapses the formidable expression (7.27) of the cubic coefficient c in the scaled center manifold dynamics (1.8), along these lines, to become

$$(7.30) \quad c = d - 2.$$

Conversely, for given $c > -2$, we can now invoke (7.29), (7.18), and (7.16), successively, to determine the parameters of the 2-cluster singularity as

$$(7.31) \quad d = c + 2, \quad \gamma' = \sqrt{3}(c + 1).$$

Since (7.29) is in fact quadratic, we may in fact replace any occurrence of $\sqrt{3}$, here and below, by $-\sqrt{3}$. For brevity, we will only address the positive sign.

At $\lambda = 0$, relations (7.18) then determine the original parameters β, γ as

$$(7.32) \quad \beta = (c + 1) - i \frac{1}{\sqrt{3}}(c + 3)$$

$$(7.33) \quad \gamma = \frac{1}{\sqrt{3}}(2c + 3).$$

Insertion of (7.31) in (7.25) and (7.26), respectively, determines the modest expressions

$$(7.34) \quad B = -\frac{8}{3}(c+1)^2(c^2+3c+3)/(2+c),$$

$$(7.35) \quad C = Bc.$$

Of course we may just as well invoke (7.33), anytime, to alternatively express all other parameters in terms of the soft/hard spring constant γ of (7.1), at the 2-cluster singularity.

In the language of section 6, each size ratio $\alpha = N_1 : N_3$ gives rise to up to three particular nonzero bifurcation values of the parameter λ in the scaled center manifold dynamics (1.8): the red saddle-node value λ_{minmax} of (4.11) and the two blocking values λ_ι , $\iota = 0, 1$ of (5.5), (5.7). To recover the meaning for the full set of coefficients λ, A, B, C in the general, unscaled center manifold setting (1.10), we just have to revert the scaling (1.11). The parameter values λ in (1.10), which correspond to each of the above reference values λ_ι , $\iota \in \{\text{minmax}, 0, 1\}$, for fixed α , are then given by the asymptotic parabolas

$$(7.36) \quad \lambda = (\lambda_\iota(\alpha)/B)A^2 + \dots$$

Higher order terms in A go beyond our third order truncation of the flow (1.10) in the center manifold, and also account for dependencies of the coefficients A, B, C on λ . This shows how all bifurcation curves emanate from the 2-cluster singularity at $A = 0, \lambda = 0$, with horizontal tangent and curvatures given by the one remaining coefficient c and the size ratios α .

See [KFHK20] for numerical illustrations of the 2-cluster singularity, in the special case of $N = 16$ Stuart-Landau oscillators (7.1) with $\gamma = 2$. Specifically, size ratios $\alpha = N_1/(N - N_1)$, $N_1 = 1, \dots, 8$ are addressed there. By (7.33), the value $\gamma = 2$ corresponds to the simplest case $c = \sqrt{3} - 3/2 > -1/2$ of section 6, as illustrated for $c = 1$ in fig. 6.8. The complex value of the coupling constant β at the 2-cluster singularity follows from (7.32).

In conclusion, we have gone beyond the discussion of 2-cluster equilibria and their stability. In fact, we have indicated rebel heteroclinic dynamics between them, in the limit of large N . For each of the seven complementary intervals of the cubic coefficient c in the center manifold dynamics (1.8), we have represented the resulting heteroclinic rebel dynamics of section 5, between the two large clusters (N_1, ξ_1) and (N_3, ξ_3) , in figures 6.1–6.8 of section 6, respectively. Since $N \rightarrow +\infty$ is finite, in practice, we have to interpret these figures on the grid of rational values $\alpha/(\alpha + 1) = N_1/N$, of course, for cluster sizes $N_1 = 0, \dots, N$. See figures 5.1, 5.2 for the appropriate interpretation of heteroclinic rebel transitions. All seven cases admit 2-cluster singularities. Indeed, even case 6.1, $c < -2$, of negative 2-cluster singularity discriminants $d = c + 2$ occurs, albeit at the expense of a repelling center manifold with transverse eigenvalue $\mu_- = -2(c + 2) > 0$; see (7.17). In the setting (7.1) of coupled Stuart-Landau oscillators, this establishes and explains the transient rebel dynamics of single oscillators between the two large clusters of synchronization, as observed by [KHK19].

References

- [BVB97] V.N. Belykh, N.N. Verichev, and I.V. Belykh. Regular and chaotic spatially homogeneous oscillations of a 1-d array of coupled Josephson junctions. *Radio-physics and Quantum Electronics* **40** (1997), 609–617.
- [ChHa82] S.-N. Chow and J.K. Hale. *Bifurcation Theory*. Springer-Verlag, New York 1982.
- [Carr] J. Carr. *Applications of Centre Manifold Theory*. Springer-Verlag, New York 1982.
- [DN04] H. Daido and K. Nakanishi. Aging transition and universal scaling in oscillator networks. *Phys. Rev. Lett.* **93** (2004), 104101.
- [DN06] H. Daido and K. Nakanishi. Diffusion-induced inhomogeneity in globally coupled oscillators: Swing-by mechanism. *Phys. Rev. Lett.* **96** (2006), 054101.
- [Elm01] T. Elmhirst. *Symmetry and Emergence in Polymorphism and Sympatric Speciation*. PhD Thesis, Warwick 2001.
- [GMK08] V. García-Morales and K. Krischer. Normal-form approach to spatiotemporal pattern formation in globally coupled electrochemical systems. *Phys. Rev. E* **78** (2008), 057201.
- [GoSt86] M. Golubitsky and I. Stewart. *Singularities And Groups in Bifurcation Theory 2*. Springer-Verlag, New York 1986.
- [GoSt02] M. Golubitsky and I. Stewart. *The Symmetry Perspective*. Birkhäuser, Basel 2002.
- [GuHo83] J. Guckenheimer and P. Holmes. *Nonlinear Oscillations, Dynamical Systems, and Bifurcations of Vector Fields*. Springer-Verlag, New York 1983.
- [HGK19] M.J. Hankins, V. Gaspar and I.Z. Kiss. Abrupt and gradual onset of synchronized oscillations due to dynamical quorum sensing in the single-cathode multi-anode nickel electrodisolution system. *Chaos* **29** (2019).
- [HR92] V. Hakim and W.-J. Rappel. Dynamics of the globally coupled complex ginzburg-landau equation. *Phys. Rev. A* **46** (1992), R7347–R7350.
- [KFHK20] F. Kemeth, B. Fiedler, S.W. Haugland, and K. Krischer. 2-cluster fixed-point analysis of mean-coupled Stuart-Landau oscillators in the center manifold of the Benjamin-Feir instability. Preprint 2020.
- [KHK19] F.P. Kemeth, S.W. Haugland, and K. Krischer. Cluster singularity: The unfolding of clustering behavior in globally coupled Stuart-Landau oscillators. *Chaos* **29** (2019).
- [KK&al14] H. Kori, Y. Kuramoto, S. Jain, I.Z. Kiss and J.L. Hudson. Clustering in globally coupled oscillators near a Hopf bifurcation: Theory and experiments. *Phys. Rev. E* **89** (2014).
- [Kri01] K. Krischer. New directions and challenges in electrochemistry - Spontaneous formation of spatiotemporal patterns at the electrode vertical bar electrolyte interface. *J. Electroanalyt. Chem.* **501** (2001), 1–21.

- [KGO15] W. Lim Ku, M. Girvan, and E. Ott. Dynamical transitions in large systems of mean field-coupled landau-stuart oscillators: Extensive chaos and cluster states. *Chaos* **25** (2015), 123122.
- [LSMK18] Y. Liu, M. Sebek, F. Mori, and I.Z. Kiss. Synchronization of three electrochemical oscillators: From local to global coupling. *Chaos* **28** (2018).
- [MGMK09] I. Miethe, V. Garcia-Morales and K. Krischer. Irregular subharmonic cluster patterns in an autonomous photoelectrochemical oscillator. *Phys. Rev. Lett.* **102** (2009).
- [MMS91] P.C. Matthews, R.E. Mirollo and S.H. Strogatz. Dynamics of a large system of coupled nonlinear oscillators. *Physica D: Nonlinear Phenomena* **52** (1991), 293 – 331.
- [MS90] P.C. Matthews and S.H. Strogatz. Phase diagram for the collective behavior of limit-cycle oscillators. *Phys. Rev. Lett.* **65** (1990), 1701–1704.
- [NK93] N. Nakagawa and Y. Kuramoto. Collective chaos in a population of globally coupled oscillators. *Progress of Theoretical Physics* **89** (1993), 313–323.
- [NK94] N. Nakagawa and Y. Kuramoto. From collective oscillations to collective chaos in a globally coupled oscillator system. *Physica D: Nonlinear Phenomena* **75** (1994), 74 – 80.
- [NK95] N. Nakagawa and Y. Kuramoto. Anomalous Lyapunov spectrum in globally coupled oscillators. *Physica D: Nonlinear Phenomena* **80** (1995), 307 – 316.
- [NKV19] J.A. Nogueira, K. Krischer and H. Varela. Coupled dynamics of anode and cathode in proton-exchange membrane fuel cells. *ChemPhysChem* **20** (2019), 3081–3088.
- [PadM82] J. Palis and W. de Melo. *Geometric Theory of Dynamical Systems*. Springer-Verlag, New York 1982.
- [PBA10] H.G. Purwins, H.U. Boedeker and Sh. Amiranashvili. Dissipative solitons. *Advances in Physics* **59** (2010), 485–701.
- [PH&al17] M. Patzauer, R. Hueck, A. Tosolini, K. Schoenleber and K. Krischer. Autonomous oscillations and pattern formation with zero external resistance during silicon electrodisolution. *Electrochimica Acta* **246** (2017), 315–321.
- [PLK04] F. Plenge, YJ Li, and K Krischer. Spatial bifurcations in the generic N-NDR electrochemical oscillator with negative global coupling: Theory and surface plasmon experiments. *J. Phys. Chem. B* **108** (2004), 14255–14264.
- [PR15] A. Pikovsky and M. Rosenblum. Dynamics of globally coupled oscillators: Progress and perspectives. *Chaos* **25** (2015), 097616.
- [PRK03] A. Pikovsky, M. Rosenblum and J. Kurths. *Synchronization: A Universal Concept in Nonlinear Sciences*, volume 12. Cambridge University Press, 2003.
- [Sch01] E. Schöll. *Nonlinear Spatio-Temporal Dynamics and Chaos in Semiconductors*, volume 10. Cambridge University Press, 2001.

- [SEC03] I. Stewart, T. Elmhirst and J. Cohen. Symmetry-breaking as an origin of species. In *Bifurcation, Symmetry and Patterns*, J. Buescu et al (eds.), Birkhäuser, Basel, 2003, 3–54.
- [SF89] M. Shiino and M. Frankowicz. Synchronization of infinitely many coupled limit-cycle type oscillators. *Physics Letters A* **136** (1989), 103–108.
- [SK15] L. Schmidt and K. Krischer. Chimeras in globally coupled oscillatory systems: From ensembles of oscillators to spatially continuous media. *Chaos* **25** (2015).
- [SZHK14] K. Schoenleber, C. Zensen, A. Heinrich and K. Krischer. Pattern formation during the oscillatory photoelectrodissolution of n-type silicon: turbulence, clusters and chimeras. *New Journal of Physics* **16** (2014).
- [Van82] A. Vanderbauwhede. *Local Bifurcation and Symmetry*. Pitman, Boston 1982.
- [Van89] A. Vanderbauwhede. Centre manifolds, normal forms and elementary bifurcations. In *Dynamics Reported* **2**, U. Kirchgraber and H.O. Walther (eds.), Vieweg+Teubner, Wiesbaden, 1989.
- [VBBK05] H Varela, C Beta, A Bonnefont, and K Krischer. A hierarchy of global coupling induced cluster patterns during the oscillatory H₂-electrooxidation reaction on a Pt ring-electrode. *PCCP* **7** (2005), 2429–2439.
- [VG&al] P. Virtanen, R. Gommers & al. SciPy 1.0: Fundamental algorithms for scientific computing in Python. *Nature Methods* **17** (2020), 261–272.
- [WKH00] W. Wang, I.Z. Kiss, and J.L. Hudson. Experiments on arrays of globally coupled chaotic electrochemical oscillators: Synchronization and clustering. *Chaos* **10** (2000), 248–256.